

Plasma Diagnostics for Planetary Nebulae and H II Regions Using the N II and O II Optical Recombination Lines

I. A. McNabb^{1*}, X. Fang², X.-W. Liu^{1,2}, R. J. Bastin^{3†} & P. J. Storey³

¹*Kavli Institute for Astronomy and Astrophysics, Peking University, Beijing 100871, China*

²*Department of Astronomy, School of Physics, Peking University, Beijing 100871, P. R. China*

³*Department of Physics and Astronomy, University College London, London WC1E 6BT, UK*

Accepted 2012 October 24. Received 2012 October 24; in original form 2012 August 10

ABSTRACT

We carry out plasma diagnostic analyses for 123 planetary nebulae (PNe) and 42 H II regions using the N II and O II optical recombination lines (ORLs). New effective recombination coefficients for the N II and O II optical recombination spectra are used. These data were calculated under the intermediate coupling scheme for a number of electron temperature (T_e) and density (N_e) cases. We used a new method to determine the T_e 's and N_e 's for the nebular sample, combining the ORLs with the most reliable measurements for each ion and the predicted intensities that are based on the new atomic data. Uncertainties of the derived T_e and N_e are estimated for each object.

The diagnostic results from heavy element ORLs show reasonable agreement with previous calculations in the literature. We compare the electron temperatures derived from the N II and O II ORLs, $T_e(\text{ORLs})$, and those from the collisionally excited lines (CELs), $T_e(\text{CELs})$, as well as the hydrogen Balmer jump, $T_e(\text{H I BJ})$, especially for the PNe with large abundance discrepancies. Temperatures from He I recombination lines, $T_e(\text{He I})$, are also used for comparison if available. For all the objects included in our sample, $T_e(\text{ORLs})$ are lower than $T_e(\text{H I BJ})$, which are in turn systematically lower than $T_e(\text{CELs})$. Nebulae with $T_e(\text{He I})$ available show the relation $T_e(\text{ORLs}) \leq T_e(\text{He I}) \leq T_e(\text{H I BJ}) \leq T_e(\text{CELs})$, which is consistent with predictions from the bi-abundance nebular model postulated by Liu et al. (2000).

Key words: atomic data – planetary nebulae: general – H II regions

1 INTRODUCTION

Photoionized nebulae, such as planetary nebulae (PNe) and H II regions, provide much of our knowledge of elemental abundances in the Milky Way and other galaxies. Accurate measurements of electron temperatures (T_e) and densities (N_e) are essential for reliable determination of elemental abundances. Until recently, the principal means of determining elemental abundances in nebulae has been from the measurement of collisionally excited lines (CELs). The emissivities of these lines relative to a hydrogen line are very sensitive to T_e under typical physical conditions of photoionized nebulae, and thus are much affected by the errors in electron temperatures. These electron temperatures are in turn derived from the traditional method based on the CEL ratios (Osterbrock & Ferland 2006), such as the [O III]

$\lambda 4363/(\lambda 4959 + \lambda 5007)$ and [N II] $\lambda 5755/(\lambda 6548 + \lambda 6584)$ nebular-to-auroral line ratios.

An alternative method of nebular abundance determinations is to ratio the intensity of an optical recombination line (ORL) of helium or a heavy element with that of hydrogen. Unlike CELs, such as the [O III] and [N II] nebular lines, whose emissivities relative to a hydrogen recombination line increase exponentially with T_e , the emissivities of heavy element ORLs relative to a hydrogen recombination line change weakly with both T_e and N_e , as the emissivities of recombination lines have only a similar, power-law dependence on T_e and N_e , apart from the parentage effects to be discussed in Section 2.2, and are essentially independent of N_e under typical nebular physical conditions (e.g. Liu 2006a, b). Consequently, the method based on ORLs is much less affected by temperature measurement errors, and the results in principle should be more conclusive. It is possible to use the intensity ratio of two ORLs originating from the recombination of different ion parents to estimate N_e (Fang, Storey & Liu 2011), since the density sensitivity

* E-mail: imcnabb@pku.edu.cn (IAM)

† Current Address: Surbiton High School, Surbiton Crescent, Kingston upon Thames, Surrey, KT1 2JT, UK

of the parent populations is partially reflected in the resultant ORL relative intensities.

While emissivities of heavy element ORLs have only a relatively weak, power-law dependence on T_e , this dependence varies for lines originating from levels of different orbital angular momentum quantum number l . Therefore, the relative intensities of ORLs can be used to derive electron temperature, provided that very accurate measurements can be secured (Liu 2003; Liu et al. 2004; Tsamis et al. 2004). Since the sensitivity of the ORL ratios to electron temperature and density is very weak, in order to obtain T_e 's and N_e 's of the nebular regions where ORLs arise, one needs to acquire high-precision measurements of these ORLs. However, given the low nebular abundances of heavy elements ($\sim 10^{-4}$ – 10^{-3} or even lower relative to hydrogen) and the relatively long time scales for a heavy element ion to recombine with an electron under the physical conditions of gaseous nebulae (Osterbrock & Ferland 2006), the heavy element ORLs are very weak compared to the CELs and low-order hydrogen lines. Therefore, high-precision measurements of those ORLs are required.

Although several deep spectroscopic surveys have been carried out during the past decade for several dozen Galactic disk and Bulge PNe (Tsamis et al. 2003b, 2004; Liu et al. 2004; Robertson-Tessi & Garnett 2005; Wesson et al. 2005; Wang & Liu 2007) and for a number of Galactic and extragalactic H II regions (Esteban et al. 2002, 2004; Tsamis et al. 2003a; Peimbert et al. 2004; García-Rojas et al. 2004, 2005, 2006), most of the ORL measurements are still not accurate enough for nebular analysis, due to either relatively low signal-to-noise ratios or line blending. Currently only a limited number of objects (mainly nearby Galactic PNe) have deep enough spectra for recombination line analysis (e.g. Liu et al. 1995, 2000, 2001; Esteban et al. 1999, 2004; Sharpee et al. 2004; Zhang et al. 2005a; Fang & Liu 2011).

In nebular astrophysics, there has been a long-standing dichotomy in abundance determinations and plasma diagnostics. For a given PN, the abundances of heavy-element ions (C^{2+} , N^{2+} , O^{2+} , and Ne^{2+}) relative to hydrogen derived from the nebular ORLs are all higher than the corresponding abundance values derived from their CEL counterparts. The electron temperatures derived from the H I Balmer jump are also systematically lower than those derived from the CELs. A number of mechanisms have been proposed to explain this dichotomy (e.g. Peimbert 1967; Rubin 1989; Viegas & Clegg 1994), but have failed to provide a consistent interpretation of all observations, especially for those PNe with dramatically large abundance discrepancies (e.g. >10 , 20). A bi-abundance nebular model postulated by Liu et al. (2000) provides a more natural explanation of this dichotomy. In this model, the ORLs heavy element ions arise mainly from “cold” H-deficient inclusions, while the strong CELs are emitted predominantly from the warmer ambient ionised gas of “normal” (\sim solar values) chemical composition. Deep spectroscopic surveys (e.g. Tsamis et al. 2003b, 2004; Liu et al. 2004; Robertson-Tessi & Garnett 2005; Wesson et al. 2005; Wang & Liu 2007) and ORL analysis of individual nebulae in the past decade (e.g. Liu et al. 1995, 2000, 2001, 2006a) have yielded strong evidence for the existence of such a “cold” component (Recent reviews on this topic are given by Liu 2003, 2006b, 2011). More re-

cently, Nicholls et al. (2012) proposed that a κ -distribution for electron energies, which is a departure from the conventional assumption of a Maxwell-Boltzmann equilibrium energy distribution, can explain the dichotomy in both H II regions and PNe.

Despite the paucity of high-quality observational data of the heavy element ORLs as well as the lack of the atomic data that are adequate enough for nebular analysis, plasma diagnostics have been carried out for a number of PNe and preliminary results have been obtained. Using the radiative recombination coefficients of Péquignot et al. (1991), Tsamis et al. (2004) derived electron temperatures using the O II ORLs for 6 Galactic PNe, and found an average T_e (O II ORLs) value of 2920 ± 2690 K. Liu et al. (2004) derived T_e (O II ORLs) for 18 PNe, and found an average value of 4910 ± 4060 K. Wesson et al. (2005) derived electron temperatures for a dozen Northern Galactic PNe using the O II ORL ratios $\lambda 4075/\lambda 4089$, $\lambda 4649/\lambda 4089$, $\lambda 4072/\lambda 4089$, $\lambda 4414/\lambda 4089$ and $V1/\lambda 4089$. Wang & Liu (2007) determined T_e (O II ORLs) for 11 Galactic PNe using the O II $\lambda 4089/\lambda 4649$ line ratio, and gave an average value of 4370 ± 5760 K. However, many of the recombination line intensities used for diagnostics were not corrected for line blending, and the derived electron temperatures could be problematic.

In this paper, we present a new approach to plasma diagnostics using the N II and O II ORLs for a sample of PNe and H II regions, which are selected from previous optical recombination line surveys and individual-object studies. The most recent effective recombination coefficients are utilised for the analysis. For each ion, we use one set of detected ORLs with the most reliable measurements to constrain T_e and N_e simultaneously, by comparing the observed intensities with the predicted ones. The primary purpose of the current paper is to show that the plasma diagnostic method employed here is applicable to all emission nebulae, provided that more and more accurate measurements of the N II and O II ORLs are available in the future.

2 OPTICAL RECOMBINATION LINE DIAGNOSTICS

In this section, we compare the intensities of the observed N II and O II lines with theoretical predictions over a wide range of electron temperatures and densities.

2.1 Planetary nebula and H II region sample

During the past two decades, several deep optical spectroscopic surveys have been carried out and published for several dozens of Galactic disk, Bulge and Halo PNe and for a number of Galactic and extragalactic H II regions. These allow for detailed nebular plasma diagnostics and abundance analyses using the relatively weak hydrogen and helium recombination lines/continua and ORLs from heavy element ions. In total, over 100 PNe and 40 H II regions have been studied using ORLs. The current paper makes use of the samples from the literature listed in Tables 1 and 2.

High spectral and spatial resolution spectroscopy of PNe has been published in the literature for detailed analysis

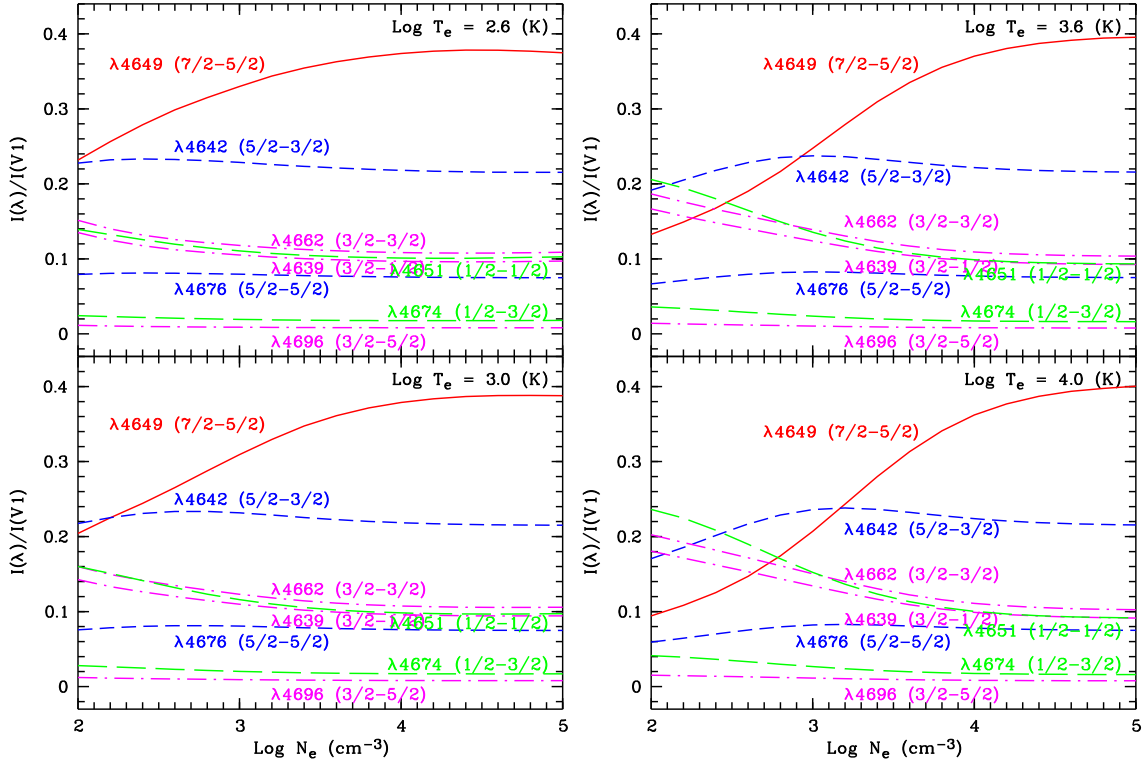


Figure 1. Theoretical fractional intensities of O II Multiplet M1: $2s^22p^23p^4D^o - 2s^22p^23s^4P$ as a function of electron density. The numbers in the brackets ($J_2 - J_1$) following the line labels are the total angular momentum quantum numbers from the upper to the lower levels. Transitions from the upper levels with the same angular momentum quantum number J_2 are represented by the curves with the same colour and line type. Four temperature cases, $\log T_e$ [K] = 2.5, 3.0, 3.5 and 4.0, are presented. The figure is based on the unpublished calculations of Storey.

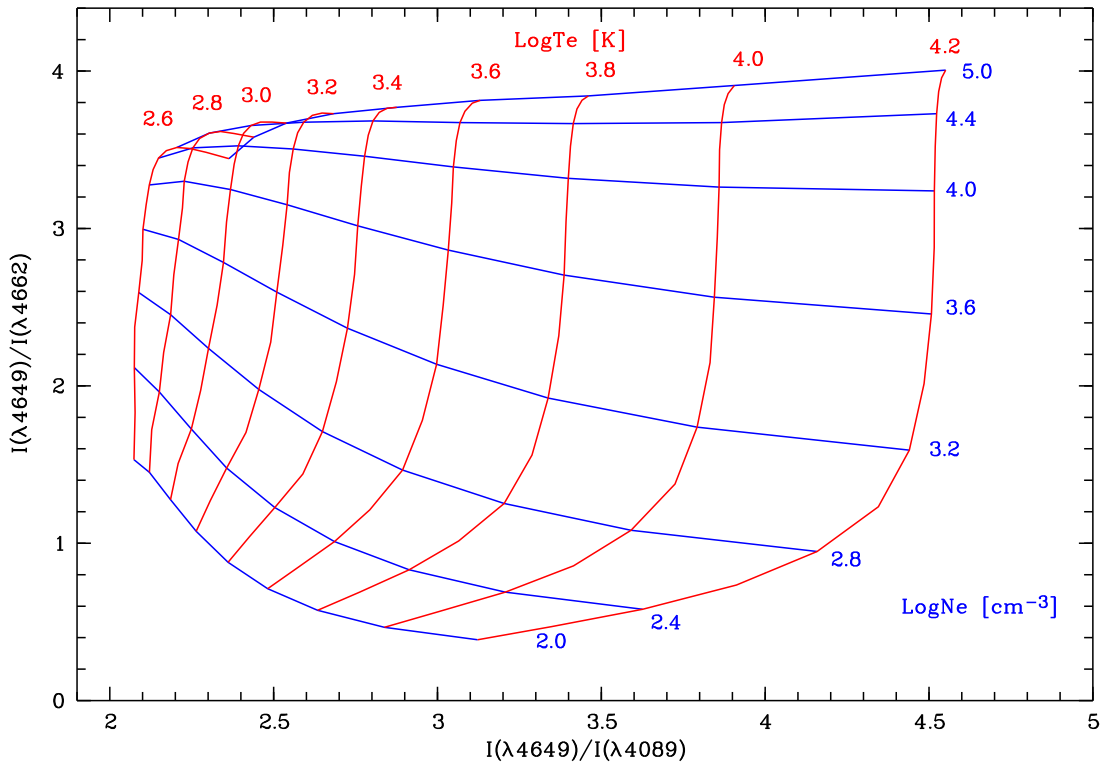


Figure 2. Loci of the O II recombination line ratios $I(\lambda 4649)/I(\lambda 4662)$ and $I(\lambda 4649)/I(\lambda 4089)$ for different T_e 's and N_e 's. The figure is based on the unpublished calculations of Storey.

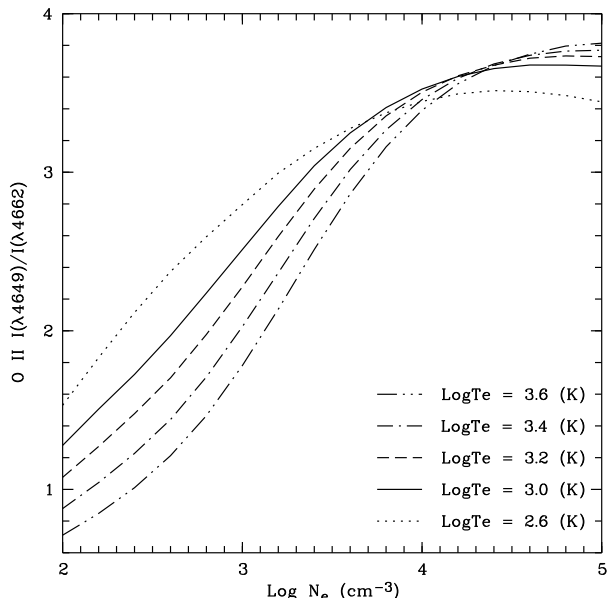


Figure 3. The O II $\lambda 4649/\lambda 4662$ recombination line ratio as a function of electron density. Different curves represent different temperature cases. The plot is based on the unpublished calculations of P. J. Storey.

of the physical condition and elemental abundance distributions across the nebulae. Tsamis et al. (2008) carried out a dedicated study of three Galactic PNe (NGC 5882, NGC 6153 and NGC 7009) by means of optical integral field spectroscopy using the Fibre Large Array Multi Element Spectrograph on the Very Large Telescope (VLT/FLAMES). The ratio of the abundances derived from ORLs and CELs, which is called the abundance discrepancy factor (ADF), was studied across the nebulae for doubly-ionised oxygen, O^{2+} . Very small values of the temperature fluctuation parameter t^2 (defined by Peimbert 1967, 1971) in the plane of the sky were found in all three objects. Most recently, Mesa-Delgado et al. (2012) published results from integral field spectroscopy of a field located near the Trapezium Cluster in the Orion Nebula using the Potsdam Multi-Aperture Spectrophotometer (PMAS). Detailed studies of one of the three most prominent protoplanetary disks (proplyds) show that the ADF of O^{2+} is close to one in the proplyd, while the background emission still yields the typical ADF(O^{2+}) observed in the Orion nebula.

2.2 Atomic data

Since the 1990s, it has been possible to obtain reliable measurements of the faint ORLs emitted by heavy element ions for bright nebulae. However, atomic data are necessary to analyse these spectral features, in particular the effective recombination coefficients. ORL ratios from states of different orbital angular momenta do show some temperature dependence and therefore can be used to measure the average temperature under which the lines are emitted (e.g. Liu 2003).

Relative populations of the fine-structure levels of the ground term of a recombining ion, such as N^{2+} in the case of N II and O^{2+} in the case of O II, deviate from the Boltzmann distribution and vary as a function of electron density

in low-density nebulae. This variation in the level population is reflected in the emissivities, and thus in the effective recombination coefficients of the recombination lines that are formed from different parent levels. In essence, the intensity ratio of two such lines can be used to determine electron density (e.g. Fang, Storey & Liu 2011).

High-precision quantum mechanical calculations of the effective recombination coefficients for N II (Fang, Storey & Liu 2011), and O II lines (Storey, unpublished) have been completed. Both calculations improve those from previous work (e.g. Nussbaumer & Storey 1984; Escalante & Victor 1990; Péquignot et al. 1991; Storey 1994; Liu et al. 1995; Kisielius et al. 1998; Kisielius & Storey 2002). The strongest and best-observed lines for N II so far have been those from multiplets V3 $3p^3D - 3s^3P^o$ and V39a,b $4fG[7/2,9/2] - 3d^3F^o$. For O II, they are from multiplets V1 $3p^4D^o - 3s^4P$, V10 $3d^4F - 3p^4D^o$, and V48a,b $4fG[5,4]^o - 3d^4F$ for O II.

Fig. 1 shows the theoretical fractional intensities of the fine-structure components of the O II Multiplet V1 $2p^23p^4D^o - 2p^23s^4P$ as a function of electron density at four temperature cases. The same can be seen for the N II multiplet V3 $2p3p^3D - 2p3s^3P^o$ in Fig. 5 from Fang, Storey & Liu (2011). Fig. 2 shows the loci of the O II recombination line ratios $I(\lambda 4649)/I(\lambda 4662)$ and $I(\lambda 4649)/I(\lambda 4089)$ for different T_e 's and N_e 's. The same can be seen for N II recombination line ratios $I(\lambda 5679)/I(\lambda 5666)$ and $I(\lambda 5679)/I(\lambda 4041)$ in Fig. 8 from Fang, Storey & Liu (2011). Using the accurate measurements of the N II and O II line ratios, we can determine T_e 's and N_e 's simultaneously from the loci. Since different ORL ratios of N II or O II have different sensitivity on T_e and N_e , this will affect the reliability of the results.

Given the different temperature-dependence of diagnostic lines, individual diagnostic line ratios are expected to yield differing results if the nebulae are not isothermal. While the small values of t^2 appear to suggest there are no large temperature variations where the CELs are emitted, the discrepancies between the CEL and ORL diagnostic results definitely exist, thereby suggesting that the gas is not isothermal. While the authors believe that the bi-abundance nebular model is a satisfactory explanation of the abundance (and temperature) discrepancies, an alternative explanation involving non-equilibrium electron energies has also been proposed (Nicholls et al. 2012; Owocki & Scudder 1983). According to Nicholls et al. (2012), physical processes such as magnetic reconnection, injection of high-energy electrons through photoionization by a "hard" photon spectrum, may generate such non-equilibrium electrons. The role of shockwaves in generating the discrepancies also needs to be explored. The choice of abundance discrepancy model, however, does not impact on the validity of the ORL diagnostics proposed here.

The traditional method, which uses one line ratio to determine an electron temperature or a density, has the disadvantage that the density or temperature is undefined. Although a temperature-sensitive recombination line ratio is usually quite insensitive to electron density, some density-sensitive line ratios, to a noticeable extent, may vary with electron temperature. As an example, Fig. 3 shows the O II $\lambda 4649/\lambda 4662$ ratio as a function of electron density. From the Figure one can see that at low densities

($\log T_e < 3.6$), the electron density yielded by the observed line ratio may differ by as much as 0.6 dex when the logarithmic temperature $\log T_e$ increases from 2.6 to 3.6. Instead of using a single line ratio, we present our new method using one set of N II or O II ORLs to constrain the electron temperature and density simultaneously. Our method is based on the fact that the intensity ratio of two of these selected ORLs is temperature-sensitive, while the ratio of the other (two) lines of this group should be density-sensitive.

2.3 Theoretical intensities

For the N II effective recombination coefficients (Fang, Storey & Liu 2011), $\log T_e$ [K] covers a range of 2.1 to 4.3, with an incremental step of 0.1, and $\log N_e$ [cm^{-3}] spans from 2.0 to 6.0, with an incremental step of 0.1. For the O II effective recombination coefficients (Storey, unpublished), $\log T_e$ [K] covers a range of 2.6 to 4.2, with an incremental step of 0.2, and $\log N_e$ [cm^{-3}] spans from 2.0 to 5.0, with an incremental step of 0.2. Both theoretical and observed intensities are normalised such that $H\beta = 100$.

For most objects, the other O II multiplets are not as strong as those considered in Figs. 1 and Fig. 2, and are not suitable to constrain T_e and N_e , due to data quality. Figs. 4 and 5 show the emissivities of N II V3 and V39 ORLs (V3 $\lambda 5666$, V3 $\lambda 5679$, V39b $\lambda 4041$ and V39a $\lambda 4035$) and O II V1 and V48 ORLs (V1 $\lambda 4649$, V1 $\lambda 4662$, V48a $\lambda 4089$ and V48c $\lambda 4087$), respectively, as a function of T_e and N_e , where the emissivity is derived from the effective recombination coefficients as follows:

$$\varepsilon(\lambda) = \alpha_{\text{eff}}(\lambda) \times \frac{hc}{\lambda}, \quad (1)$$

with h as Planck's constant and c as the speed of light, all in cgs units. Due to coarse grid resolution, we performed a bilinear interpolation on the effective recombination coefficients of the O II ORLs provided by Storey (unpublished). Bilinear interpolation simply extends linear interpolation for functions of two variables, i.e. $\alpha_{\text{eff}}(T_e, N_e)$.

Based on the calculations of the effective recombination coefficients for the N II and O II lines, theoretical intensity for an N II or O II ORL relative to $H\beta$ can be calculated as a function of T_e and N_e as follows:

$$I_{\text{pred}}(\lambda) = \frac{I(\lambda)}{I(H\beta)} = \frac{\alpha_{\text{eff}}(\lambda)}{\alpha_{\text{eff}}(H\beta)} \frac{4861}{\lambda} \frac{X^+}{H^+} \times 100, \quad (2)$$

where $I_{\text{pred}}(T_e, N_e)$ is the theoretical predicted intensity of the transition λ , normalised such that $I(H\beta) = 100$. $\alpha_{\text{eff}}(\lambda; T_e, N_e)$ is the effective recombination coefficient for the transition λ , and $\alpha_{\text{eff}}(H\beta; T_e, N_e)$ is the effective recombination coefficient for $H\beta$, which is adopted from the hydrogenic calculations of Storey & Hummer (1995). The ionic abundances relative to hydrogen derived from ORLs, X^+/H^+ , can be found in the literature for each nebula.

If the spectral resolution for the nebula is relatively poor, for instance $\text{FWHM} < 1.5 \text{ \AA}$, then some blending may occur. The theoretical intensities from the blended lines are then added together in the following manner:

$$\sum_{i=1}^n I_{\text{pred}}(\lambda_i) = \sum_{i=1}^n \left(\frac{\alpha_{\text{eff}}(\lambda_i)}{\lambda_i} \right) \frac{4861}{\alpha_{\text{eff}}(H\beta)} \frac{X^+}{H^+} \times 100, \quad (3)$$

where i goes from 1 to the number of the blended lines.

2.4 Plasma diagnostics

2.4.1 Least-squares fit

For each PN and H II region, the aforementioned theoretical intensities were compared with the observed intensities using a least-squares minimisation method as follows:

$$\chi^2 = \sum_{i=1}^n \left(\frac{I_{\text{obs}}(\lambda_i) - I_{\text{pred}}(\lambda_i)}{I_{\text{pred}}(\lambda_i)} \right)^2, \quad (4)$$

where χ^2 is the sum over the combination of n lines used for either N II or O II, as a function of T_e and N_e . I_{obs} is the observed intensity for the transition λ_i and I_{pred} is the predicted intensity. For a blended feature, the observed intensity is compared with the combined theoretical intensities of the blended lines, described in Eqn. (3). As an example, Figs. 6 and 7 show the $\log \chi^2$ distributions for 4 PNe (Hf 2-2, M 1-42, NGC 6153 and NGC 7009) for N II and O II, respectively. The location of the minimum $\log \chi^2$ value can be determined for each comparison, thus providing the optimal ($\log T_e, \log N_e$), as shown by the white cross hairs in both figures.

2.4.2 Error estimate

For many objects, the resulting temperatures and densities are well confined. However, it is difficult to decide how reliable these diagnostic results could be. Not all of the surveys or individual detailed studies of PNe and/or H II regions provided errors along with their observational intensities. This makes estimating the uncertainties for the optimal ($\log T_e, \log N_e$) rather complicated. A few nebulae had observational errors presented in the literature and are adopted in the current analyses. For those nebulae whose measurement uncertainties are not presented in the literature, we estimated errors according to their observational conditions and data quality. In order to determine the uncertainties for the optimal ($\log T_e, \log N_e$), we carried out an extra set of calculations that begin with random number generation.

For each line in a combination of N II or O II ORLs (e.g. V3 $\lambda 5666$, V3 $\lambda 5679$, V39a $\lambda 4035$, and V39b $\lambda 4041$ for N II, and V1 $\lambda 4662$, V1 $\lambda 4649$, V48a $\lambda 4089$, and V48c $\lambda 4087$ for O II) that are used for plasma diagnostics, we used IDL to generate a number, N_{sim} , of intensity values, $I_{\text{sim}}(\lambda_i)$, with a normal (Gaussian) distribution centred around the original observational intensity, $I_{\text{obs}}(\lambda_i)$, along with a standard deviation obtained from the observational error, $\sigma(I_{\text{obs}})$, of this distribution.

The mean intensities of the simulations and standard deviations, $I_{\text{sim}}^{\text{mean}}$ and $\sigma(I_{\text{sim}}^{\text{mean}})$, are calculated as follows:

$$I_{\text{sim}}^{\text{mean}} = \frac{\sum_{i=1}^{N_{\text{sim}}} I_{\text{sim}}^i(\lambda)}{N_{\text{sim}}}, \quad (5)$$

and

$$\sigma(I_{\text{sim}}^{\text{mean}}) = \sqrt{\frac{\sum_{i=1}^{N_{\text{sim}}} (I_{\text{sim}}^i(\lambda) - I_{\text{sim}}^{\text{mean}})^2}{N_{\text{sim}}}}, \quad (6)$$

The standard deviation of these generated numbers also agree well with the observational errors. Each combination

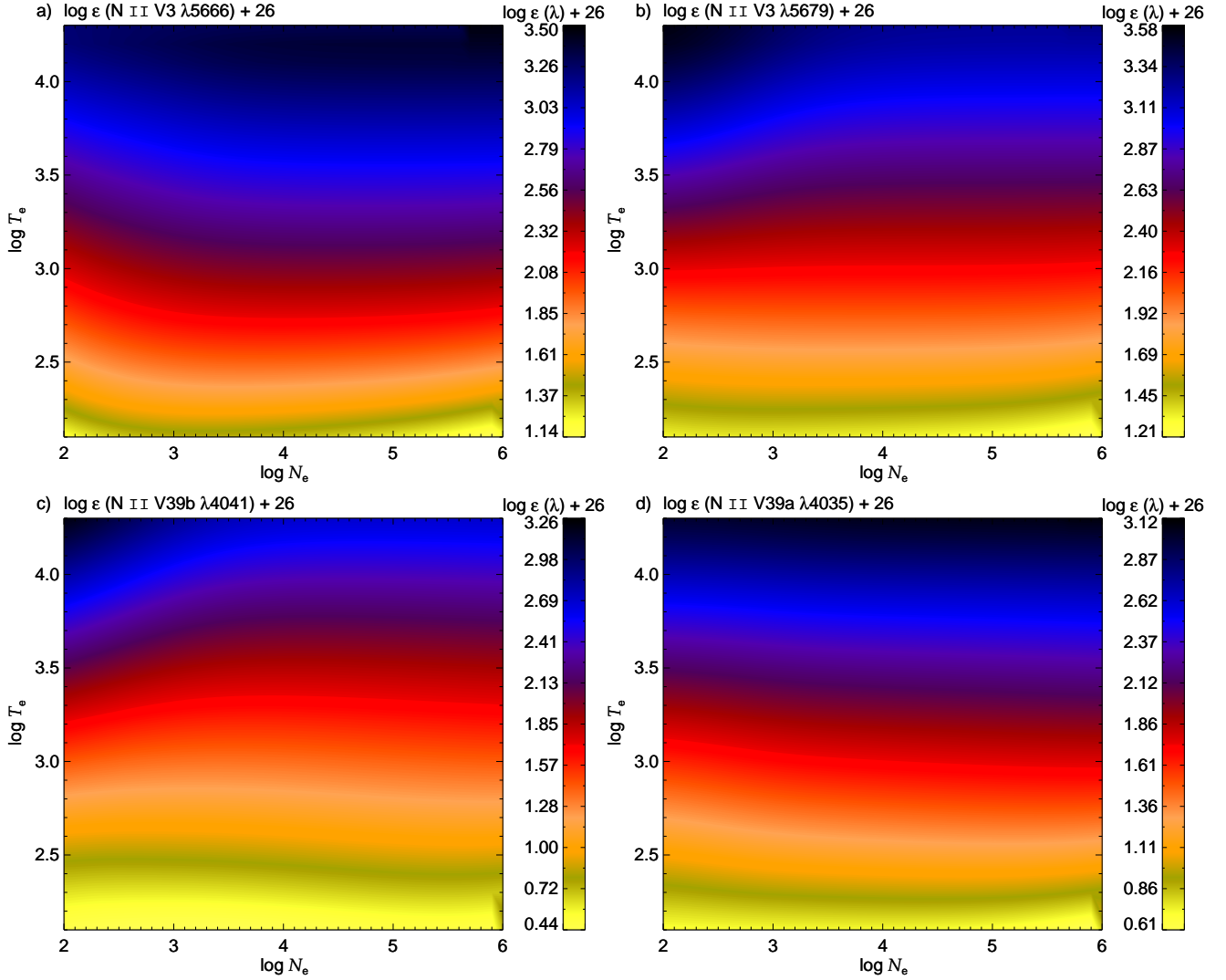


Figure 4. Emissivities of the N II a) V3 $\lambda 5666$, b) V3 $\lambda 5679$, c) V39b $\lambda 4041$ and d) V39a $\lambda 4035$ lines as a function of electron temperature and density, as derived by Eqn. (1). The colour bar indicates the $\log \varepsilon(\lambda) + 26$ values in units of $\text{ergs cm}^{-3} \text{s}^{-1}$.

of the randomly generated line intensities, $I_{\text{sim}}^i(\lambda)$, where i is from 1 to N_{sim} , is used to determine a unique optimal $(\log T_e, \log N_e)$, following the method described in Section 2.4.1.

Errors of the optimal $\log T_e$ and $\log N_e$ of each nebula are then calculated from these N_{sim} temperatures and densities, which can be denoted as T_e^i and N_e^i , where $i = 1, \dots, N_{\text{sim}}$. For those objects whose $\log T_e - \log N_e$ diagram shows multiple peaks, standard deviations of T_e and N_e are calculated, which are centred on the mean values of these N_{sim} temperatures and densities. The random intensities of each ORL are then normally distributed within the observational errors of the observed intensities. The program would then calculate the $\log \chi^2$ along the entire T_e and N_e grid for each combination of the random intensities and determine the minimum value, thus deriving the unique optimal $(\log T_e, \log N_e)$ for that simulation.

Figs. 8 and 9 display the frequencies of these optimal $\log T_e$ and $\log N_e$ distributions for the N II and O II ORLs, respectively, for the same 4 PNe shown in Figs. 6 and 7. The errors for the optimal $\log T_e$ and $\log N_e$ are derived as follows:

$$T_{\text{sim}}^{\text{mean}} = \frac{\sum_{i=1}^{N_{\text{sim}}} T_e^i}{N_{\text{sim}}}, \quad (7)$$

and

$$N_{\text{sim}}^{\text{mean}} = \frac{\sum_{i=1}^{N_{\text{sim}}} N_e^i}{N_{\text{sim}}}, \quad (8)$$

with respective standard deviations calculated as follows:

$$\sigma(T_{\text{sim}}^{\text{mean}}) = \sqrt{\frac{\sum_{i=1}^{N_{\text{sim}}} (T_e^i - T_{\text{sim}}^{\text{mean}})^2}{N_{\text{sim}}}}, \quad (9)$$

and

$$\sigma(N_{\text{sim}}^{\text{mean}}) = \sqrt{\frac{\sum_{i=1}^{N_{\text{sim}}} (N_e^i - N_{\text{sim}}^{\text{mean}})^2}{N_{\text{sim}}}}. \quad (10)$$

These values are represented in Figs. 8 and 9 as green error bars centred at $T_{\text{sim}}^{\text{mean}}$ and $N_{\text{sim}}^{\text{mean}}$, but projected on the white crosshairs of the optimal $\log T_e$ and $\log N_e$ locations obtained from observations, thus providing upper and lower limits. The white solid contour designates the 1- σ level around the peak. We project the standard deviations onto

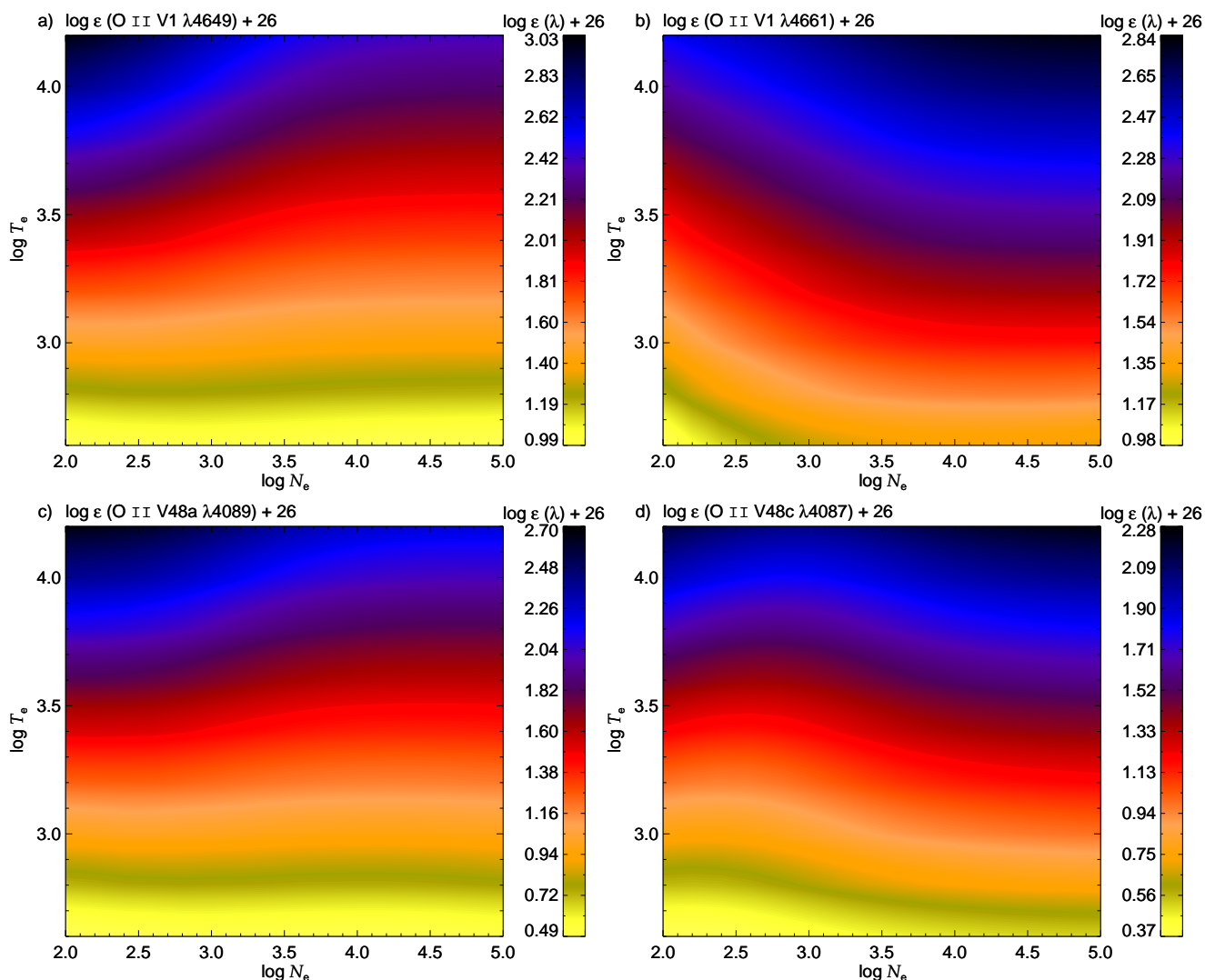


Figure 5. The same as Figure 4, but for O II a) V1 $\lambda 4649$, b) V1 $\lambda 4662$, c) V48a $\lambda 4089$ and d) V48c $\lambda 4087$ lines.

the optimal $\log T_e$ and $\log N_e$ locations obtained from observations because they are calculated using the $1-\sigma$ errors of the observed intensities.

3 RESULTS AND DISCUSSION

3.1 Temperature structure of photoionized nebulae

Figs. 10 and 11 show the electron temperatures from the literature and the current ORL diagnostics for 46 PNe and for 42 H II regions, respectively. The PNe in Fig. 10 were chosen out of the whole list because they met the following criteria: 1) $T_e([\text{O III}])$, $T_e(\text{H I})$ and $T_e(\text{He I})$ are available from literature, 2) $2.6 < \log T_e(\text{O II ORLs}) < 4.2$ and/or 3) $2.1 < \log T_e(\text{N II ORLs}) < 4.3$. For the PNe plotted in Fig. 10, the mean value of $\log T_e([\text{O III}])$ is 4.01 ± 0.09 [K] (red solid line). The mean value of $\log T_e(\text{H I BJ})$ is 3.91 ± 0.29 [K] (orange dotted line). The mean value of $\log T_e(\text{He I } \lambda 7281/\lambda 6678)$ is 3.67 ± 0.19 [K] (purple dashed line). The mean value of $\log T_e(\text{O II ORLs})$ is 3.22 ± 0.52 [K] (green dot-dashed line). The mean value of $\log T_e(\text{N II ORLs})$ is 3.20 ± 0.59 [K] (blue dot-dot-dot-dashed line). In the case of the PNe,

the mean values clearly show the temperature sequence: $T_e(\text{ORLs}) \leq T_e(\text{He I}) \leq T_e(\text{H I}) \leq T_e(\text{CELs})$, which is consistent with predictions from the bi-abundance model (Liu et al. 2000; Liu 2003). While the physical conditions of the main nebula and cold, H-deficient component may vary from nebula to nebula, over all the nebulae there is a general trend that many contain a secondary cold, H-deficient component.

For the H II regions plotted in Fig. 11, the mean value of $\log T_e([\text{O III}])$ is 4.00 ± 0.11 [K] (red solid line). The mean value of $\log T_e(\text{H I BJ})$ is 3.87 ± 0.08 [K] (orange dotted line). The mean value of $\log T_e(\text{He I } \lambda 7281/\lambda 6678)$ is 3.91 [K] (purple dashed line). The mean value of $\log T_e(\text{O II ORLs})$ is 3.24 ± 0.57 [K] (green dot-dashed line). The mean value of $\log T_e(\text{N II ORLs})$ is 3.15 ± 0.87 [K] (blue dot-dot-dot-dashed line). In the case of the H II regions, the mean values show the temperature relation: $T_e(\text{ORLs}) \leq T_e(\text{H I}) \leq T_e(\text{He I}) \leq T_e(\text{CELs})$. The difference in this relation are most likely due to the faint nature and large measurement errors of He I lines in some of the H II regions.

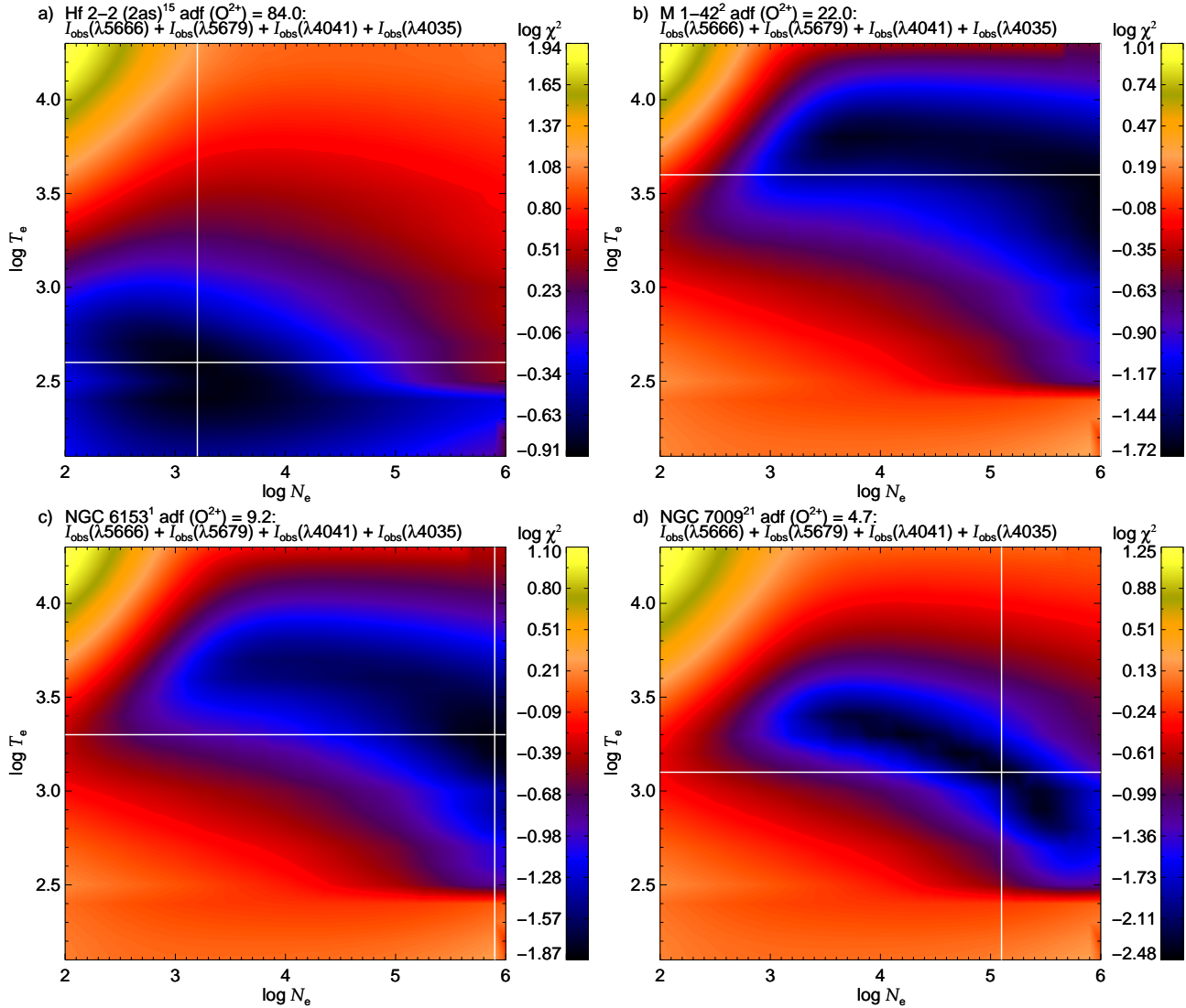


Figure 6. $\log \chi^2(T_e, N_e)$ distributions for N II V3 5666, V3 5679, V39b 4041 and V39a 4035 over the entire $\log T_e - \log N_e$ grid for 4 PNe. The white crosshair pinpoints the absolute minimum χ^2 value for the N II line combinations indicating the optimal $\log T_e$ and $\log N_e$. The colour bars indicate the $\log \chi^2$ values. ADF values are from literature: a) Hf2-2¹(Liu et al. 2006), b) M 1-42²(Liu et al. 2001), c) NGC 6153¹⁵(Liu et al. 2000), and d) NGC 7009²¹(Fang & Liu 2011).

3.2 Physical evolution of photoionized nebulae

Fig. 12 shows histograms of $T_e([\text{O III}])$, $T_e(\text{H I BJ})$, $T_e(\text{He I})$, $T_e(\text{O II})$ and $T_e(\text{N II})$, for PNe (blue) and H II regions (red). The He I ORL temperatures are derived from the line ratio $\lambda 7281/\lambda 6678$ using the fitting functions of Zhang et al. (2005b). Given the weakness of the N II and O II ORLs, the large scatter seen in the $T_e(\text{O II})$ and $T_e(\text{N II})$ distributions are most likely due to observational uncertainties. The diagram clearly shows the relation of the average temperatures for the PNe, $T_e(\text{ORLs}) \leq T_e(\text{He I}) \leq T_e(\text{H I}) \leq T_e(\text{CELs})$, which is also seen in Fig. 10. The average T_e 's and standard deviations are labelled for PNe (in red) and H II regions (in blue). Many PNe and H II regions in our analysis show $T_e(\text{O II})$ lower than 2.6 and $T_e(\text{N II})$ lower than 2.1, the lowest T_e 's for which the effective recombination coefficients are available, respectively, although only a handful of H II regions had N II ORLs listed in their literature for us to perform our diagnostics. As can be seen in Fig. 11, the temperature histograms of [O III] CELs, He I, H I BJ, O II and

N II ORLs show an increase in the width of the distributions from [O III] through N II. This can be either caused by the observational uncertainties arising from increasingly difficult measurements, especially for the extremely faint ORLs or possibly due to variations of physical properties of the cold H-deficient inclusions and main nebula from object to object, causing the scatter in $T_e(\text{N II})$ and $T_e(\text{O II})$.

Fig. 13 shows the ADF (O^{2+}/H^+) versus $T_e([\text{O III}]) - T_e(\text{H I BJ})$, for PNe (blue) and H II regions (red). The 123 PNe analysed here are shown as the blue open circles; amongst them the 46 PNe plotted in Fig. 10 are shown as the blue filled circles. A linear least-squares fit to the 46 PNe from Fig. 10 with reliable electron temperatures indicates a positive correlation. The PNe shown in open circles and H II regions are not considered for the linear fit. This most likely indicates a tight correlation between the ADF of a nebulae and the temperature discrepancy. The 42 H II regions analysed here are shown as the red open squares with 40 H II regions shown as red closed squares if they had positive N II or O II $\log T_e$ results. The H II regions plotted in

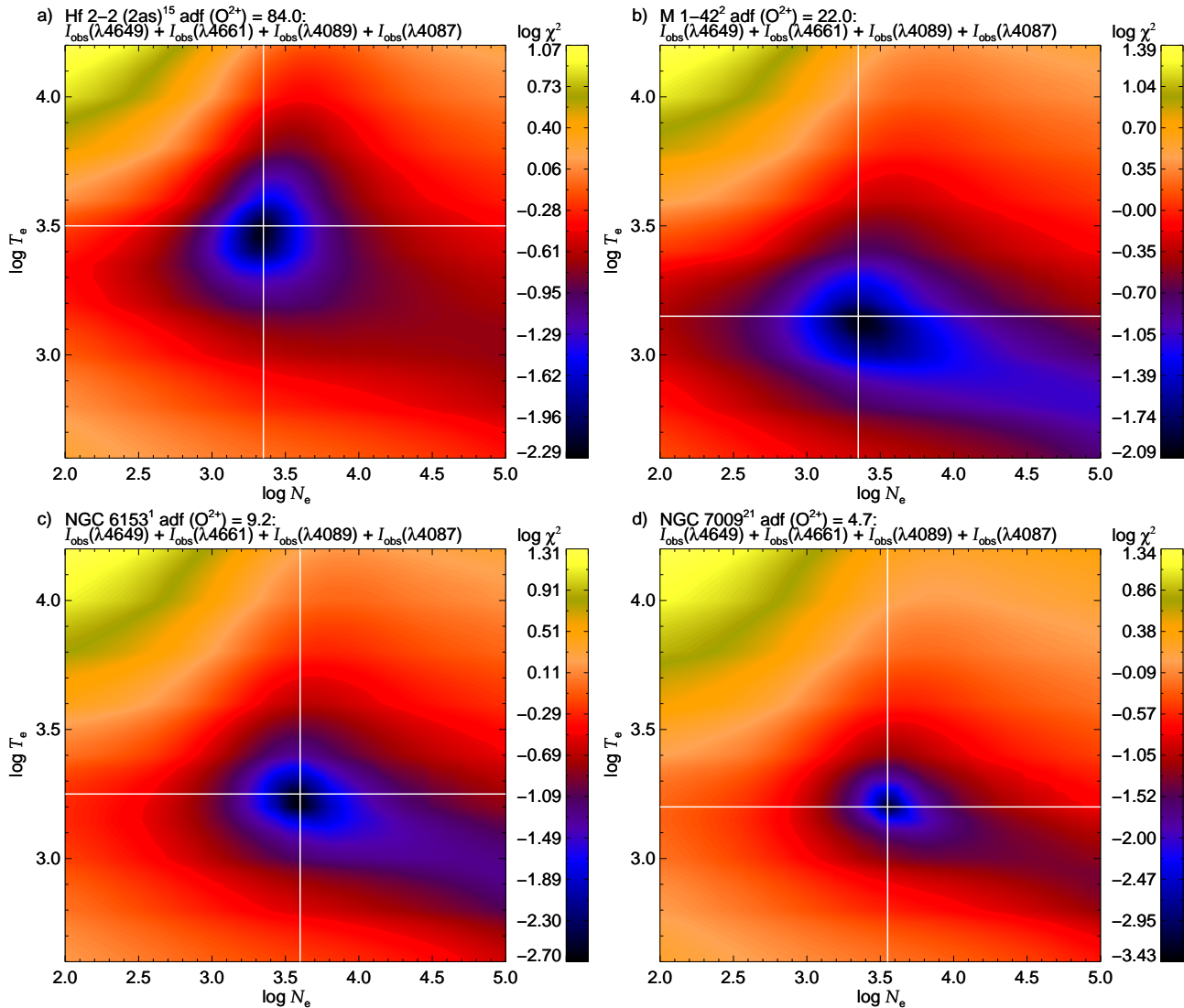


Figure 7. The same as Fig. 6 but for O II V1 4649, V1 4662, V48a 4089 and V48c 4087 lines over the entire $\log T_e$ - $\log N_e$ grid for the same 4 PNe.

Fig. 13 just show large scatter, making it difficult to determine if there is a correlation between the ADF value and temperature discrepancy.

The nebulae with lower ADF values might be relatively young in their evolution processes when the main nebulae are very bright, and therefore the cold, H-deficient components might be mixed with the main nebula, and the effects of the cold, H-deficient components are insignificant. However, for the nebulae with high ADF values, the nebula might have expanded such that the main nebula has a relatively low surface brightness compared to the condensed, cold H-deficient condensations, thus making it easier to distinguish the two based on the temperatures derived from CELs and those derived from ORLs. Therefore for most PNe, there may be an evolution from younger, more compact nebulae where the cold, H-deficient component is embedded and almost indistinguishable from the main bright nebula to older, more diffuse nebulae where the fainter main nebula distinctly envelopes the cold, H-deficient condensations.

3.3 Comments on several archetypal planetary nebulae

3.3.1 Hf2-2

There are several well-studied planetary nebulae that have been observed for many decades. Hf2-2 is a well-known southern PN, that has an unusually high ADF (O^{2+}) value of 84 (Liu et al. 2006). They observed this PN with the ESO 1.52-m telescope with three separate slit widths of 2, 4, and 8 arcsec, using the 2-arcsec width for maximum spectral resolution. Hf2-2 is known to have a close binary system with a very short orbital period (0.398 days, Lutz et al. 1998). It has also shown a very peculiar nature and may be included in the 'born-again' PNe scenario, relating the particularly large ADF to the phenomenon of novae, as stated in Wesson et al. (2003). From their 2-arcsec slit-width observations, Liu et al. (2006) derived the following electron temperatures: $T_e([\text{O III}]) = 8710$, $T_e(\text{He I } \lambda 6678/\lambda 5876) = 1570$, and $T_e(\text{H I}) = 933$ K. From the plasma diagnostics based on the N II ORL lines of V3 45666, V3 45679, V39b 44041, V39a 44035, we derived an electron temperature of 398^{+9}_{-135} K, as shown in the first panels of Fig. 5 for the χ^2 minimisa-

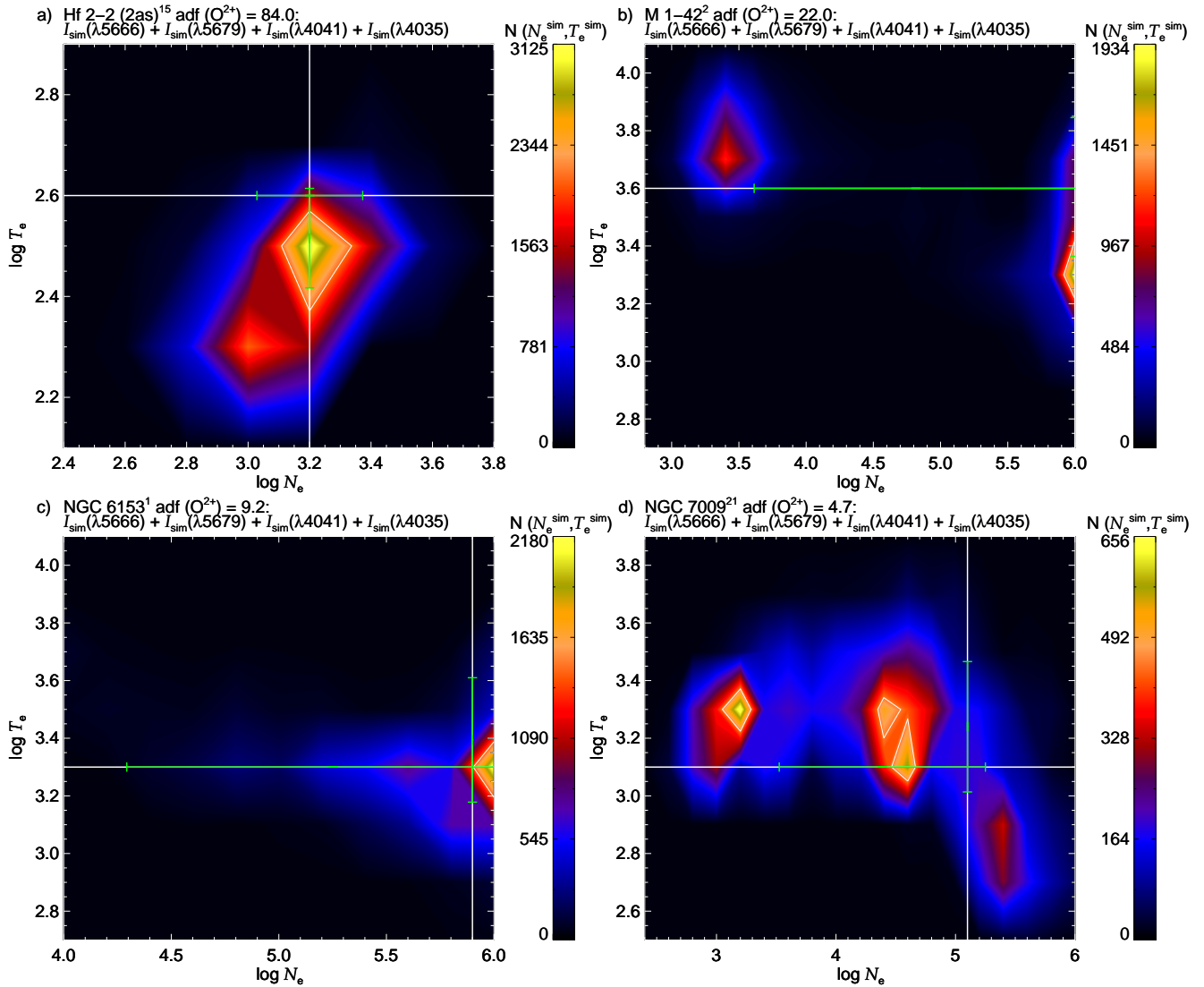


Figure 8. 2-dimensional frequencies of the optimal $\log T_e$ and $\log N_e$ locations calculated from 10 000 simulations within a 1- σ normal (Gaussian) distribution for N II V3 $\lambda 5666$, V3 $\lambda 5679$, V39b $\lambda 4041$ and V39a $\lambda 4035$ over a portion of the $\log T_e$ - $\log N_e$ grid for the same 4 PNe as Figs 5 and 6, sorted by descending ADF. The white crosshair pinpoints the optimal $\log T_e$ and $\log N_e$ location obtained from the observed intensities. The light-green error bars also show the standard deviations as derived from Eqn. 6. The ADF values are adopted from literature: a) Hf2-2¹ (Liu et al. 2006), b) M 1-42² (Liu et al. 2001), c) NGC 6153¹⁵ (Liu et al. 2000), and d) NGC 7009²¹ (Fang & Liu 2011).

tion and Fig. 8 for the standard deviations. From the plasma diagnostics based on the O II ORLs of V1 $\lambda 4649$, V1 $\lambda 4661$, V48a $\lambda 4089$, V48c $\lambda 4087$, we derived an electron temperature of 3160_{-820}^{+730} K, as shown in the first panels of Fig. 7 for the χ^2 minimisation and Fig. 9 for the standard deviations.

3.3.2 M 1-42

Another PN is the Galactic bulge nebula M 1-42, which was first discovered by Minkowsky (1946). More recently, Liu et al. (2001) observed M 1-42 along with M 2-36 using the ESO 1.52-m telescope. For M 1-42 they derived a fairly high ADF of 22. Liu et al. (2001) derived the following electron temperatures: $T_e([\text{O III}]) = 9120$ K, $T_e(\text{He I } \lambda 7821/\lambda 6678) = 3790$ K, and $T_e(\text{H I}) = 3980$ K. From our plasma diagnostics based on the N II ORLs, V3 $\lambda 5666$, V3 $\lambda 5679$, V39b $\lambda 4041$ and V39a $\lambda 4035$, we derived an electron temperature of 3980_{-1690}^{+3100} K, as shown in the

second panel of Fig. 5 for the χ^2 minimisation and Fig. 8 for the standard deviations. But as one can see in the two figures, the electron density of 10^6 cm^{-3} only provides an upper limit for the diagnostics. From our plasma diagnostics based on the O II ORLs, V1 $\lambda 4649$, V1 $\lambda 4661$, V48a $\lambda 4089$ and V48c $\lambda 4087$, we derived an electron temperature of 1410_{-150} K, as shown in the second panel of Fig. 7 for the χ^2 minimisation and Fig. 9 for the standard deviations.

3.3.3 NGC 6153

Over the last several decades, detailed studies have been put forth on the well-known planetary nebula NGC 6153, a possibly super-metal-rich nebula and first noted by Pottasch et al. (1984). Liu et al. (2000) derived a moderately high ADF of 9.2. Deduced from their electron density distribution and the optical appearance of NGC 6153, Yuan et al. (2011) suggested it is most likely a bipolar neb-

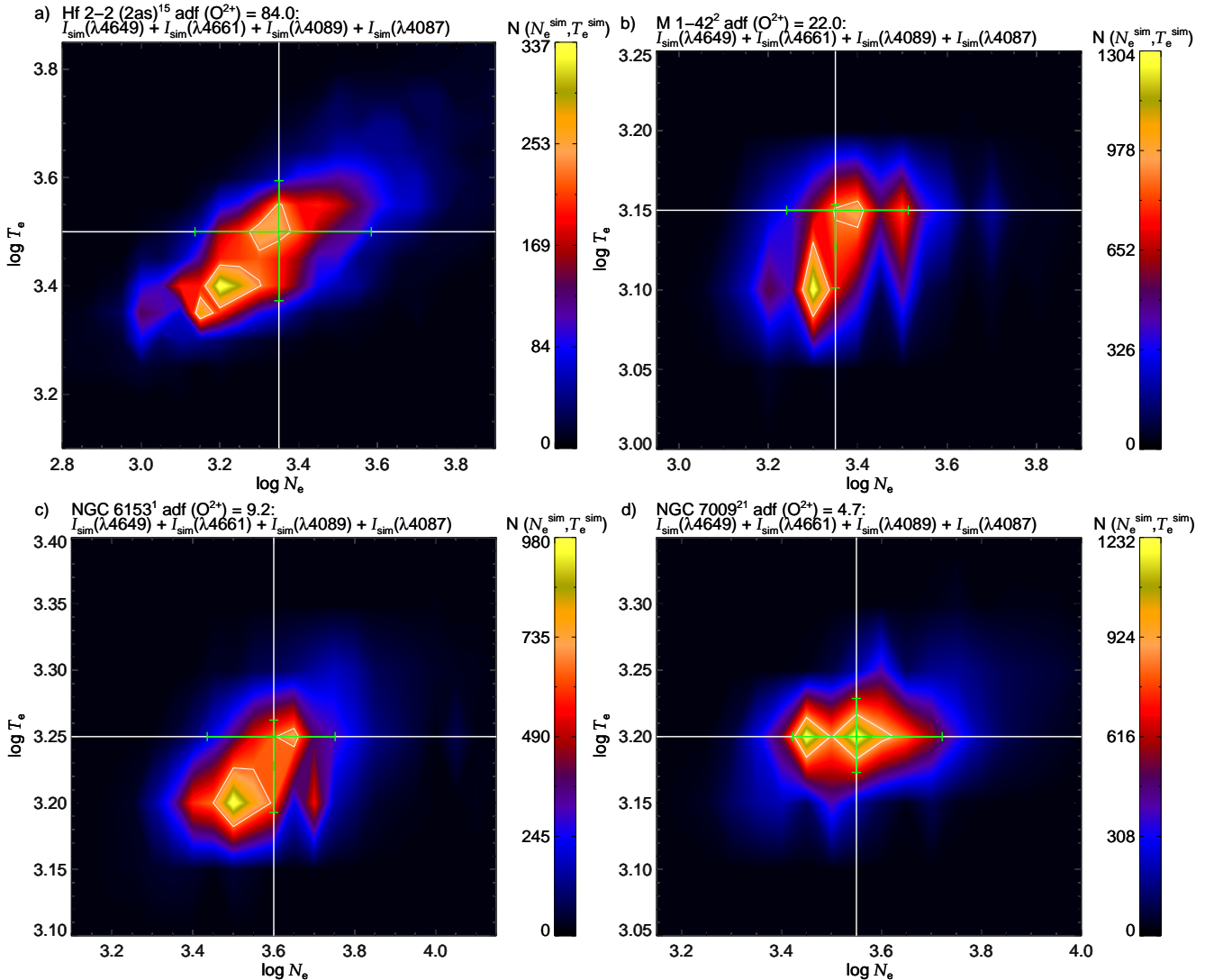


Figure 9. The same as Figure 8 but with O II V1 $\lambda 4649$, V1 $\lambda 4662$, V48a $\lambda 4089$ and V48c $\lambda 4087$ lines for the same 4 PNe.

ula probably with a central cavity and a density-enhanced waist, as viewed at a large angle to its polar axis. However, they also argue that a convincing physical model accounting for the full range of behaviour NGC 6153 exhibits is still to be found. From the strong emission lines, they derived the following electron temperatures: $T_e([\text{O III}]) = 7240$ K, $T_e(\text{He I } \lambda 7821/\lambda 6678) = 3260$ K, and $T_e(\text{H I}) = 6030$ K. Based on the N II ORLs of V3 $\lambda 5666$, V3 $\lambda 5679$, V39b $\lambda 4041$ and V39a $\lambda 4035$, our plasma diagnostics derived an electron temperature of 2000^{+2080}_{-480} K, as shown in the third panel of Fig. 6 for the χ^2 minimisation and Fig. 8 for the standard deviations. Based on the O II ORLs of V1 $\lambda 4649$, V1 $\lambda 4661$, V48a $\lambda 4089$ and V48c $\lambda 4087$, our plasma diagnostics yields an electron temperature of 1780^{+40}_{-230} K, as shown in the third panel of Fig. 7 for the χ^2 minimisation and Fig. 9 for the standard deviations.

3.3.4 NGC 7009

NGC 7009 has had hundreds of publications over the last 50 years or more. Also known as the Saturn nebula, this large, double-ringed, high-surface-brightness nebula is particularly well known for having an unusually rich and strong

O II optical permitted lines ever since the early high-resolution photographic spectroscopy observations of Wyse (1942) and Aller & Kaler (1964), having observed more than 100 O II permitted transitions (Liu et al. 1995). A much more recent work by Fang & Liu (2011) has made use of very deep CCD spectrum of the Saturn Nebula covering from 3040 to 11 000 Å. They derived a reasonably high ADF of about 5. They identified over 1000 emission lines with 81 per cent attributed to permitted lines and more than 200 O II permitted lines. Their observations were made using the ESO 1.52 m telescope and the William Herschel Telescope (WHT), and securing all spectra with a long slit. Table 3 in their paper lists a very complete set of electron temperatures and densities derived from numerous line ratios. They derived the following electron temperatures: $T_e([\text{O III}]) = 9810$ K, $T_e(\text{He I } \lambda 7821/\lambda 6678) = 5100$ K, and $T_e(\text{H I}) = 6420$ K. From our plasma diagnostics based on the N II lines of V3 $\lambda 5666$, V3 $\lambda 5679$, V39b $\lambda 4041$ and V39a $\lambda 4035$, we derived an electron temperature of 1260^{+1690}_{-235} K, as shown in the fourth panel of Fig. 6 for the χ^2 minimisation and Fig. 8 for the standard deviations. Due to the data quality, our χ^2 minimisation technique only provides an upper limit to the electron density for N II ORLs. But judging

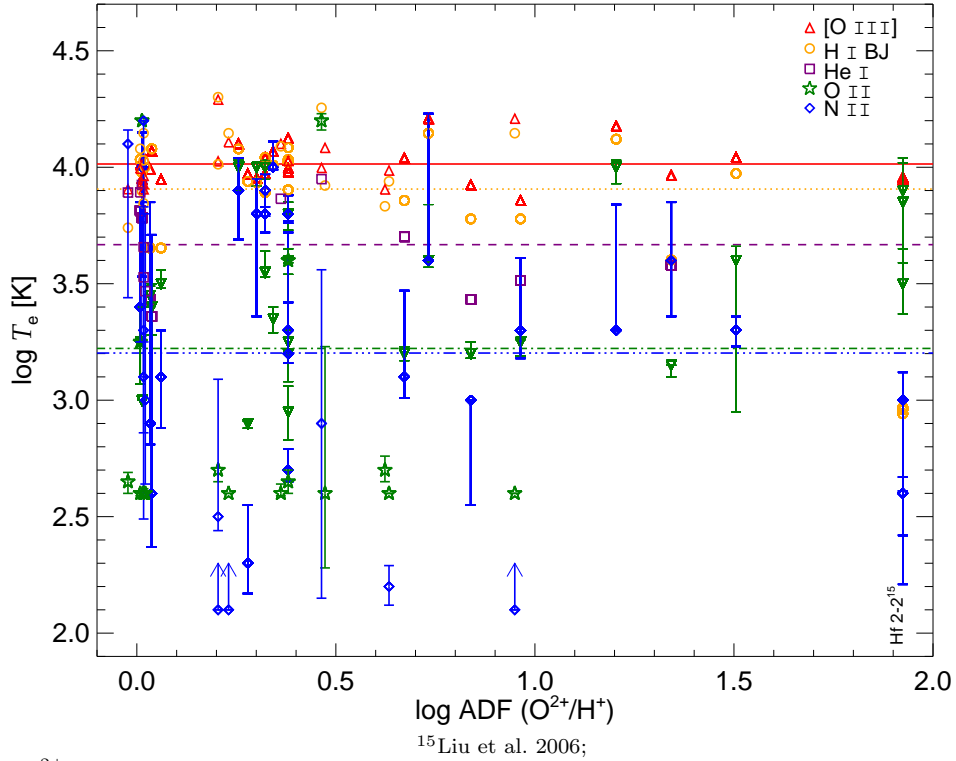


Figure 10. ADF(O^{2+}) values versus electron temperature using a variety of diagnostics for 46 PNe. Red triangles represent the $\log T_e([O \text{ III}])$ values. Orange circles represent the $\log T_e(H \text{ I BJ})$. Purple squares represent the $\log T_e(He \text{ I } \lambda 7281/\lambda 6678)$. Green stars represent the $\log T_e(O \text{ II})$ from ORL diagnostics. Blue diamonds represent the $\log T_e(N \text{ II})$ from ORL diagnostics. The red solid line indicates the mean $\log T_e([O \text{ III}])$ value. The orange dotted line indicates the mean $\log T_e(H \text{ I})$ value. The purple dashed line indicates the mean $\log T_e(He \text{ I})$ value. The green dot-dashed line indicates the mean $\log T_e(O \text{ II})$ value. The blue dot-dot-dot-dashed line indicates the mean $\log T_e(N \text{ II})$ value. The 3 PNe, Hu 1-2 (Liu et al. 2004), NGC 6790 (Robertson-Tessi & Garnett 2005) and NGC 2440 (Tsamis et al. 2004), that have $\log T_e(N \text{ II}) = 2.1$ are lower limits due to the poor quality of the data and the limited number of line intensities found in their literature.

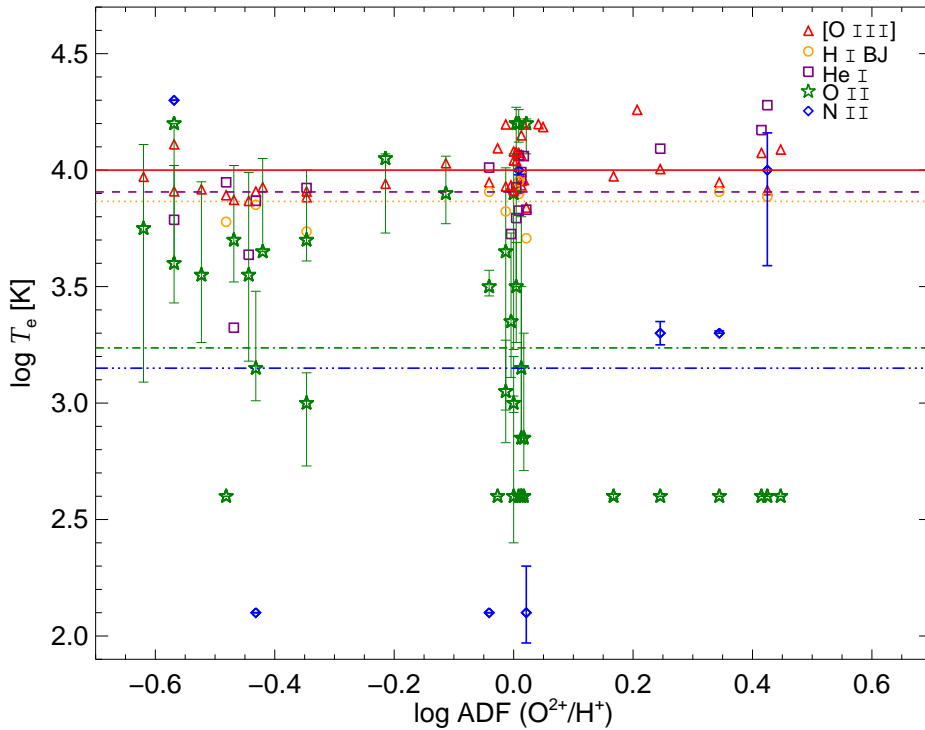


Figure 11. The same as Figure 10 but for 42 H II regions.

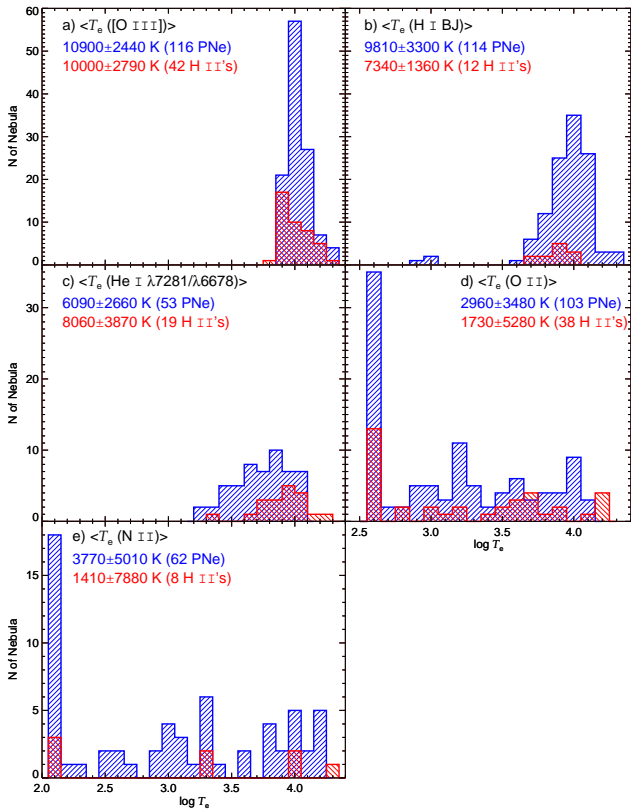


Figure 12. Distributions of T_e derived from a) [O III] CELs; b) H I Balmer Jump; c) He I line ratio $\lambda 7281/\lambda 6678$ from literature and our own calculations; d) O II ORL diagnostics; and e) N II ORL diagnostics for PNe (blue) and H II regions (red). For the distribution in each panel, the average T_e and standard deviations are labelled for PNe (blue) and H II regions (red).

from the 2-D distributions of the results derived from the randomly generated simulated intensities, a secondary peak occurs at an electron density of 1580 cm^{-3} and a temperature of 2000 K. From our plasma diagnostics based on the O II lines of V1 $\lambda 4649$, V1 $\lambda 4661$, V48a $\lambda 4089$ and V48c $\lambda 4087$, we derived an electron temperature of 1580^{+113}_{-106} K, as shown in the fourth panel of Fig. 7 for the χ^2 minimisation and Fig. 9 for the standard deviations.

3.3.5 Abell 58 & Abell 30

Another rather peculiar planetary nebula is Abell 58, a “born-again” planetary nebula, known to contain an H-deficient knot surrounding V605 Aql, according to Wesson et al. (2008). Hidden by a thick dusty torus, V605 Aql cannot be seen directly. However, from the surface abundances derived for the star from observations of its scattered light, Clayton et al. (2006) found it to be a typical Wolf-Rayet central star of PN. Wesson et al. (2008) did not measure any N II ORLs in Abell 58. From the plasma diagnostics based on the O II ORLs of V1 $\lambda 4649$, V1 $\lambda 4661$, V10 $\lambda 4075$ and V10 $\lambda 4069.62$ (blended with V10 $\lambda 4069.89$), we derived an upper limit to the electron temperature (~ 15800 K).

Wesson et al. (2003) have provided detailed optical analysis of two of the H-deficient knots (J1 & J3) in another “born-again” PN Abell 30. This nebula consists of a rather

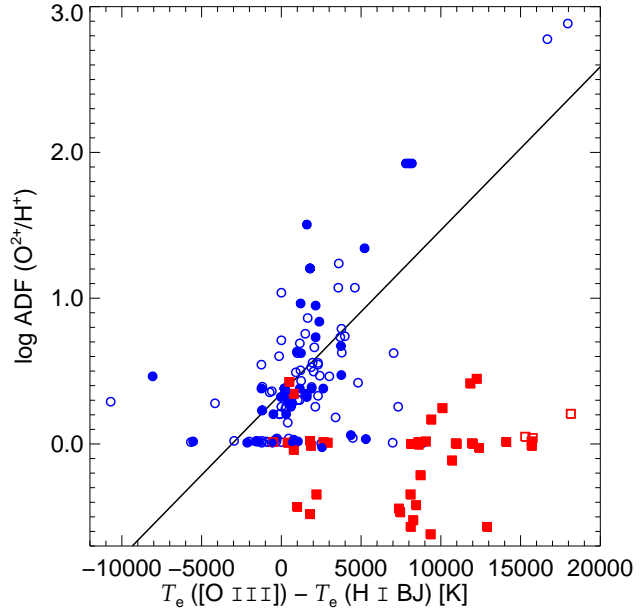


Figure 13. Log ADF (O^{2+}/H^+) versus $T_e([\text{O III}]) - T_e(\text{H I BJ})$ relation for PNe (blue) and H II regions (red). The blue open circles are all 123 PNe listed in Table 1. The blue closed circles are all the 46 PNe plotted in Fig. 10. The solid black line shows a least-squares fit to the 46 PNe plotted in Fig. 10. The red open squares are all 42 H II regions listed in Table 2. The red closed squares are H II regions with either $\log T_e(\text{O II})$ or $\log T_e(\text{N II})$ greater than zero.

large, 120 arcsec across, spherical shell of low surface brightness and several bright clumps, first discovered by Jacoby (1979) and Hazard et al. (1980), of material about 10 arcsec away from the central star. For Wesson et al. (2003), they observed Abell 30 with the 4.2 m WHT at the Observatorio del Roque de los Muchachos, on La Palma, Spain, with a 0.82 arcsec slit width. These two knots have extremely high ADF values of 598 and 766 for J1 and J3, respectively.

Wesson et al. (2003) derived the following electron temperatures for knot J1: $T_e([\text{O III}]) = 20800$ K, and $T_e(\text{He I } \lambda 5876/\lambda 4471) = 350$ K. Wesson et al. (2003) did not measure any N II ORLs in the knot J1. From the plasma diagnostics based on the O II ORLs of V1 $\lambda 4649$, V1 $\lambda 4661$, V10 $\lambda 4075$ and V10 $\lambda 4069.62$ (blended with V10 $\lambda 4069.89$), we derived an upper limit to the electron temperature (~ 15800 K). For knot J3, Wesson et al. (2003) derived the following electron temperatures: $T_e([\text{O III}]) = 17960$ K, $T_e(\text{He I } \lambda 6678/\lambda 4471) = 9240$ K. They didn’t measure any N II ORLs in this knot either. Plasma diagnostics based on the O II ORLs yielded an upper limit to the electron temperature (~ 15800 K).

3.4 Results and discussion

Tables 1 and 2 list the electron temperatures and densities for the 167 nebulae, including 123 PNe and 42 H II regions, respectively. These objects are presented in descending order of ADF (O^{2+}/H^+). Column 1 is the nebula name. Column 2 contains the ADF values from literature. Column 3 is the $\log T_e([\text{O III}])$ [K] value from literature. Column 4 is the $\log T_e(\text{BJ})$ [K] value from literature. Column 5 is the $\log T_e(\text{N II})$ [K] result from our plasma diagnostics. Column 6 is the $\log N_e(\text{N II})$ [cm^{-3}] result from our plasma

diagnostics. Column 7 is the $\log T_e(\text{O II})$ [K] result from our plasma diagnostics. Column 8 is the $\log N_e(\text{O II})$ [cm^{-3}] result from our plasma diagnostics.

Detailed modelling for the He I recombination lines have been computed for a couple decades now. Benjamin, Skillman & Smits (1999) combined the Smits (1996) models with collisional transitions of Sawey & Berrington (1993) producing accurate emissivities. More recently, Zhang et al. (2005b) applied computational models for the He I recombination lines for several dozen PNe. They also provide fitting functions spanning from 5000 to 20000 K with fitting parameters that are density-dependent.

Tables 3 and 4 show the electron temperatures derived from the He I ORLs for PNe and H II regions, respectively. The three He I line ratios $\lambda 7281/\lambda 6678$, $\lambda 6678/\lambda 4471$ and $\lambda 6678/\lambda 5876$ are used, and the objects are in descending order of the ADF values. The PN diagnostic results from Zhang et al. (2005b) are adopted. For those PNe that are not included in the sample of Zhang et al. (2005b), we derived electron temperatures using the fitting formula of Zhang et al. (2005b), and the He I line intensities are adopted from literature. Column 1 is the nebula name. Column 2 is the ADF value from literature. Columns 3 through 5 are the T_e 's derived from the He I line ratios. Most literatures provided line intensities for the four He I lines $\lambda 7281$, $\lambda 6678$, $\lambda 5876$ and $\lambda 4471$.

Resonance fluorescence may also have a minor effect on the strengths of ORLs. Grandi (1976) discussed in detail the effects of resonance fluorescence on permitted transitions. It has been known that the N II permitted lines from the low-lying 3d-3p and 3p-3s triplet arrays, whose upper levels are linked to the ground term $2p^2\ ^3P$ by resonance lines, can be enhanced by fluorescence excitation. Grandi (1976) used photoionization models to study the excitation mechanisms of permitted transitions from common heavy element ions observed in the spectra of the Orion nebula and two Galactic PNe NGC 7027 and NGC 7662.

Grandi (1976) found that while the N II M28 3d $^3D^o - 3p\ ^3P$ multiplet is excited by both recombination and continuum fluorescence of the starlight, emission of the N II M3 3p $^3D - 3s\ ^3P^o$, M5 3p $^3P - 3s\ ^3P^o$ and M30 4s $^3P^o - 3p\ ^3P$ multiplets are dominated by fluorescence excitation of the N II 4s $^3P_1^o$ level by the He I 1s8p $^1p_1^o - 1s^2\ ^1S_0$ $\lambda 508.643$ resonance line, which coincides in wavelength with the N II 2p4s $^3P_1^o - 2p^2\ ^3P_0$ $\lambda 508.668$ line. Fluorescence excitation cannot excite the singlet transitions or transitions from the 3d-4f configuration. Given the fact that measurements of the N II ORLs for the majority of nebulae samples are of relatively large uncertainty due to weakness and blend, the effects of fluorescence on the plasma diagnostic results are insignificant. For those nebulae with good observations, e.g., the several archetypal PNe discussed in Section 3.3, detailed modelling is needed to estimate the exact contribution of fluorescence mechanisms. Grandi (1976) showed that the dominant excitation mechanism of the strongest O II permitted lines is recombination.

4 SUMMARY

For nearly four decades, analyses of gaseous nebulae are mainly based on the bright CELs, whose emissivities are acutely sensitive to electron temperature (e.g. Osterbrock & Ferland 2006). Thus the abundances derived from CELs could be subject to the uncertainties caused by temperature fluctuations if present in the nebulae. The ORLs of heavy element ions, although much weaker by nature, are much less sensitive to temperature, and the resultant abundances are supposed to be more reliable, provided that very accurate measurements of the heavy element ORLs can be obtained. In the current paper, we demonstrate a new plasma diagnostic method based on the N II and O II optical recombination spectra, using the new effective recombination coefficients. This is the first work devoted to nebular analysis using heavy element ORLs, with a large sample of PNe and H II regions considered. The results show systematic differences between the electron temperatures derived from CELs, the optical recombination spectra of H I and He I, and the N II and O II ORLs. The observed temperature sequence has been found in previous observations, and is in agreement with the expectation of the bi-abundance nebular model (Liu et al. 2000). Although very deep, high-resolution spectra of gaseous nebulae, especially accurate measurements of heavy element ORLs, are still rare, we need to develop plasma diagnostic tools based on the heavy element ORLs for future study, given that the most comprehensive treatment of the N II and O II recombination under the physical conditions of gaseous nebulae (i.e., the effective recombination coefficients for the N II and O II recombination spectra) are now available. The main purpose of this paper is to demonstrate the new method of nebular analysis and show its potential application.

The method presented in the current work for determining T_e and N_e from multiple transitions of N II and O II is general and quite promising for the future deep spectroscopic studies of gaseous nebulae. Transitions from multiplets V3 and V39 for N II and from V1, V10 and V48 for O II tend to be the strongest and most reliable to constrain the χ^2 distribution over the entire $\log T_e - \log N_e$ grid. However, some other N II and O II transitions can be used as well. Therefore, this method can potentially cover broad wavelength ranges of a spectrum instead of just determining the T_e and N_e from just a couple of lines, depending on the data quality. Given that the heavy element ORLs are intrinsically faint, high signal-to-noise ratios are needed to improve the data quality.

ACKNOWLEDGMENTS

IAM thanks M. B. N. Kouwenhoven and Rubén Garca-Benito of KIAA for some helpful suggestions.

REFERENCES

- Aller, L. H. & Kaler, J., 1964, *ApJS*, **139**, 1074
 Benjamin, R. A., Skillman, E. D. & Smits, D. P. 1999, *ApJ*, **514**, 307
 Clayton, G. C., Kerber, F., Pirzkal, N., De Marco, O., Crowther, P. A. & Fedrow, J. M., 2006, *ApJ*, **646**, 69

- Ercolano, B., Wesson, R., Zhang, Y., Barlow, M. J., De Marco, O., Rauch, T. & Liu, X.-W. 2004, *MNRAS*, **354**, 558
- Escalante, V. & Victor, G. A., 1990, *ApJS*, **73**, 513E
- Esteban, C., Peimbert, M., Torres-Peimbert, S., García-Rojas, J., Rodríguez, M. 1999, *MNRAS*, **120**, 113
- Esteban, C., Peimbert, M., Torres-Peimbert, S. & Rodríguez, M., 2002, *ApJ*, **581**, 241
- Esteban, C., Peimbert, M., García-Rojas, J., Ruiz, M. T., Peimbert, A. & Rodríguez, M. 2004, *MNRAS*, **355**, 229
- Esteban, C., Bresolin, F., Peimbert, M., García-Rojas, J., Peimbert, A. & Mesa-Delgado A. 2009, *ApJ*, **700**, 654
- Fang, X., Storey, P. J., Liu, X.-W., 2011, *A&A*, **530**, A18
- Fang, X. & Liu, X.-W., 2011, *MNRAS*, **415**, 181
- García-Rojas, J., Esteban, C., Peimbert, M., Rodríguez, M., Ruiz, M. T. & Peimbert, A. 2004, *ApJS*, **153**, 501
- García-Rojas, J., Esteban, C., Peimbert, A., Peimbert, M., Rodríguez, M. & Ruiz, M. T. 2005, *MNRAS*, **362**, 301
- García-Rojas, J., Esteban, C., Peimbert, M., Costado, M. T., Rodríguez, M., Peimbert, A. & Ruiz, M. T. 2006, *MNRAS*, **368**, 253
- García-Rojas, J., Esteban, C., Peimbert, A., Rodríguez, M., Peimbert, A. & Ruiz, M. T. 2007, *Rev. Mex. Astron. Astrophys.*, **43**, 3
- García-Rojas, J., Peña, M. & Peimbert, A., 2008, *A&A*, **496**, 1
- Grandi, S., 1976, *ApJ*, **206**, 658
- Hazard, C., Terlevich, R., Ferland, G., Morton, D. C. & Sargent, W. L. W. 1980, *Nature*, **285**, 463
- Jacoby, G. H., 1979, *PASP*, **91**, 754
- Kisielius, R., Storey, P. J., Davey, A. R., & Neale, L. T., 1998, *A&AS*, **133**, 257
- Kisielius, R., & Storey, P. J., 2002, *A&A*, **387**, 1135
- Liu, X.-W., Storey, P. J., Barlow, M. J., Clegg, R.E.S., 1995, *MNRAS*, **272**, 369
- Liu, X.-W., Storey, P. J., Barlow, M. J., Danziger, I. J., Cohen, M. & Bryce, M. 2000, *MNRAS*, **312**, 585
- Liu, X.-W., Luo, S. G., Barlow, M. J., Danziger, I. J. & Storey, P. J. 2001, *MNRAS*, **327**, 141
- Liu X.-W., 2003, in Kwok S., Dopita M., Sutherland R., eds, *Proc. IAU Symp. 209, Planetary Nebulae: Their Evolution and Role in the Universe*. Astron. Soc. Pac., San Francisco, p.339
- Liu, X.-W., 2006a, in: Walsh, J., Stanghellini, L., Douglas, N., eds., *Planetary Nebulae beyond the Milky Way* (Berlin: Springer-Verlag), p.169
- Liu, X.-W., 2006b, In: Barlow, M. J., Méndez, R. H. (eds.), *Planetary Nebulae in our Galaxy and Beyond*, *Proc. IAU Symp. 234* (Cambridge: Cambridge University Press) p.219
- Liu, X.-W., Barlow, M. J., Zhang, Y., Bastin, R. J. & Storey, P. J. 2006, *MNRAS*, **368**, 1959
- Liu, X.-W., 2011, in York, D. G., Gingerich, O., Zhang, S.-N., Harper, C. L., eds, *New Vision 400: Engaging Big Questions in Astronomy and Cosmology Four Hundred Years after the Invention of the Telescope*. CRC Press, p.103
- Liu, Y., Liu, X.-W., Barlow, M. J. & Luo, S. G., 2004, *MNRAS*, **353**, 1251
- López-Sánchez, Á. R., Esteban, C., García-Rojas, J., Peimbert, M. & Rodríguez, M. 2007, *ApJ*, 656, 168
- Lutz, J. et al. 1998, *BAAS*, **30**, 894
- Minkowsky, R., 1946, *PASP*, **58**, 305
- Mesa-Delgado, A., Núñez-Díaz, M., Esteban, C., García-Rojas, J., Flores-Fajardo, N., López-Martín, L., Tsamis, Y. G. & Henney, W. J. 2012, *MNRAS*, **426**, 614
- Nicholls, D. C., Dopita, M. A. & Sutherland, R. S. 2012, *ApJ*, **752**, 148
- Nussbaumer, H. & Storey, P. J., 1984, *A&AS*, **56**, 293
- Osterbrock, D. E., Ferland, G. J. (2006). *Astrophysics of Gaseous Nebulae and Active Galactic Nuclei*. Sausalito: University Science Books.
- Owocki, S. P. & Scudder, J. D. 1983, *ApJ*, **270**, 758
- Peimbert, M., 1967, *ApJ*, **150**, 825
- Peimbert, M., 1971, *Bol. Obs. Tonantzintla y Tacubaya*, **6**, 29
- Peimbert, M., Peimbert, A., Ruiz, M. T. & Esteban, C. 2004, *ApJS*, **150**, 431
- Péquignot, D., Petitjean, P., Boisson, C., 1991, *A&A*, **251**, 680
- Pottasch, S. R., et al. 1984, *ApJ*, **278**, 33
- Rubin, R. H. 1989 *ApJS*, **69**, 897
- Robertson-Tessi, M., Garnett, D., 2005, *ApJS*, **157**, 371
- Otsuka, M., Tajitsu, A., Hyung, S., Izumiura, H., 2010, *ApJ*, **541**, 688
- Ruiz, M. T., Peimbert, A., Peimbert, M., Esteban, C., 2003, *ApJ*, **595**, 247
- Sawey, P. M. J. & Berrington, K. A. 1993, *Atomic Data and Nuclear Data Tables*, **55**, 81
- Sharpee, B., Baldwin, J. A. & Williams, R., 2004, *ApJ*, **615**, 323
- Sharpee, B., Zhang, Y., Williams, R., Pellegrini, E., Cagnolo, K., Baldwin, J. A., Phillips, M. & Liu, X.-W. 2007, *ApJ*, **659**, 1265
- Smits, D. P. 1996, *MNRAS*, **278**, 683
- Storey, P. J., 1994, *A&A*, **282**, 999
- Storey, P. J. & Hummer, D. G., 1995, *MNRAS*, **272**, 41
- Tsamis, Y. G., Barlow, M. J., Liu, X.-W., Danziger, I. J. & Storey, P. J. 2003a, *MNRAS*, **338**, 687
- Tsamis, Y. G., Barlow, M. J., Liu, X.-W., Danziger, I. J. & Storey, P. J. 2003b, *MNRAS*, **345**, 186
- Tsamis, Y. G., Barlow, M. J., Liu, X.-W., Storey, P. J. & Danziger, I. J. 2004, *MNRAS*, **353**, 953
- Tsamis, Y. G., Walsh, J. R., Péquignot, D., Barlow, M. J., Danziger, I. J. & Liu, X.-W. 2008, *MNRAS*, **386**, 22
- Viegas, S. M. & Clegg, R. E. S. 1994, *MNRAS*, **271**, 993
- Wang, W., & Liu, X.-W. 2007, *MNRAS*, **381**, 669
- Wesson, R., Liu, X.-W., Barlow, M. J. 2003, *MNRAS*, **340**, 253
- Wesson, R., & Liu, X.-W. 2004, *MNRAS*, **351**, 1026
- Wesson, R., Liu, X.-W. & Barlow, M. J. 2005, *MNRAS*, **362**, 424
- Wesson, R., Barlow, M. J., Liu, X.-W., Storey, P. J., Ercolano, B. & De Marco, O. 2008, *MNRAS*, **383**, 1639
- Wyse, A. B. 1942, *ApJ*, 95, 356
- Yuan, H.-B., Liu, X.-W., Péquignot, D., Rubin, R. H., Ercolano, B. & Zhang, Y. 2011, *MNRAS*, 411, 1035
- Zhang, Y. & Liu, X.-W., 2003, *A&A*, **404**, 545
- Zhang, Y., Liu, X.-W., Luo, S. G., Péquignot, D. & Barlow, M. J. 2005a, *A&A*, **442**, 249
- Zhang, Y., Liu, X.-W., Liu, Y., Rubin, R. H., 2005b, *MNRAS*, **358**, 457

Table 1. Electron temperatures and densities for PNe.

Object	ADF (O ²⁺)	From Literature		From Current Work			
		log T_e ([O III]) [K]	log T_e (BJ) [K]	log T_e (N II) [K]	log T_e (N II) [cm ⁻³]	log T_e (O II) [K]	log T_e (O II) [cm ⁻³]
Abell 30 J3 ²⁰	766.00	4.25 ²⁰		4.30 ^{0.01} _{0.01}	2.00	4.20	2.00
Abell 30 J1 ²⁰	598.00	4.22 ²⁰		4.30	2.00	4.20	2.00
Abell 58 ³¹	89.00					4.20	2.00
Hf 2-2 (2 arcsec) ¹⁵	84.00	3.94 ¹⁵	2.97 ¹⁵	2.60 ^{0.01} _{0.18}	3.20 ^{0.17} _{0.17}	3.50 ^{0.09} _{0.13}	3.35 ^{0.23} _{0.21}
Hf 2-2 (4 arcsec) ¹⁵	84.00	3.96 ¹⁵	2.94 ¹⁵	3.00 ^{0.12} _{0.33}	2.70 ^{1.51} _{0.65}	3.90 ^{0.14} _{0.38}	3.85 ^{0.35} _{0.57}
Hf 2-2 (8 arcsec) ¹⁵	84.00	3.95 ¹⁵	2.96 ¹⁵	3.00 ^{0.79} _{0.20}	2.30 ^{3.59} _{0.20}	3.85 ^{0.17} _{0.20}	5.00 ^{0.10} _{0.93}
NGC 1501 ⁶	32.00	4.04 ⁶	3.97 ⁶	3.30 ^{0.06} _{0.07}	6.00 ^{0.09} _{0.44}	3.60 ^{0.06} _{0.65}	3.10 ^{0.83} _{0.27}
M 1-42 ²	22.00	3.96 ²	3.60 ²	3.60 ^{0.25} _{0.24}	6.00 ^{0.92} _{2.39}	3.15 ^{0.05} _{0.11}	3.35 ^{0.16} _{0.11}
NGC 40 ⁷	17.30	4.03 ⁷	3.85 ⁷			2.60	2.00 ^{0.03} _{0.01}
M 2-24 ⁵	17.00		4.20 ⁵	2.10 ^{0.01} _{0.01}	5.70 ^{0.10} _{0.14}	4.20 ^{0.14} _{0.20}	3.80 ^{0.37} _{0.29}
NGC 2022 ⁴	16.00	4.18 ⁴	4.12 ⁴	2.10 ^{0.01} _{0.01}	5.90 ^{0.05} _{0.06}	2.60	2.00
NGC 2022 ¹⁰	16.00	4.18 ¹⁰	4.12 ¹⁰	3.30 ^{0.54} _{0.06}	6.00 ^{0.15} _{0.07}	4.00 ^{0.03} _{0.07}	3.45 ^{0.31} _{0.25}
DdDm 1 ¹³	11.80	4.09 ¹³	3.94 ¹³	4.30	2.00	3.65 ^{0.20} _{0.12}	5.00 ^{0.01} _{0.02}
Vy 2-2 ¹³	11.80	4.14 ¹³	3.97 ¹³			4.20	2.90 ^{0.02} _{0.04}
NGC 6153 ³²	10.90					3.35 ^{0.38} _{0.44}	4.45 ^{0.47} _{2.00}
NGC 6153 ¹	9.20	3.86 ¹	3.78 ¹	3.30 ^{0.31} _{0.12}	5.90 ^{0.31} _{1.61}	3.25 ^{0.01} _{0.06}	3.60 ^{0.15} _{0.16}
NGC 2440 ⁴	8.90	4.21 ⁴	4.15 ⁴	2.10	5.90	2.60	2.00
IC 2003 ¹³	7.31	4.10 ¹³	4.04 ¹³			4.20	5.00
M 2-36 ²	6.90	3.92 ²	3.78 ²	3.00 ^{0.45} _{0.10}	2.90 ^{1.84} _{0.10}	3.20 ^{0.05} _{0.02}	3.50 ^{0.11} _{0.16}
Vy 1-2 ¹³	6.17	4.02 ¹³	3.82 ¹³			3.90 ^{0.10} _{0.15}	3.65 ^{0.11} _{0.14}
NGC 3242 ⁴	5.70	4.07 ⁴	4.01 ⁴			2.60	2.00
M 3-27 ¹³	5.48	4.11 ¹³	3.96 ¹³			4.10 ^{0.09} _{0.03}	3.45 ^{0.08} _{0.06}
NGC 2440 ¹⁰	5.40	4.21 ¹⁰	4.15 ¹⁰	3.60 ^{0.63} _{0.12}	2.50	3.60 ^{0.24} _{0.03}	5.00 ^{0.14} _{0.62}
NGC 2440 ¹⁶	5.40	4.17 ¹⁶	4.04 ¹⁶	2.50 ^{1.57} _{0.12}	6.00 ^{0.08} _{1.74}	4.20	5.00 ^{0.12} _{0.99}
NGC 7009 ³²	5.14					2.95 ^{0.61} _{0.23}	5.00 ^{0.02} _{2.56}
NGC 6818 ⁴	4.90	4.12 ⁴	4.08 ⁴	2.10	5.90	2.60	2.00
NGC 7009 ²¹	4.70	4.04 ²¹	3.86 ²¹	3.10 ^{0.37} _{0.09}	5.10 ^{0.15} _{1.58}	3.20 ^{0.03} _{0.03}	3.55 ^{0.17} _{0.13}
IC 3568 ⁷	4.60	4.06 ⁷	3.97 ⁷	2.10	5.90	2.60	2.00
NGC 6210 ⁷	4.30	3.99 ⁷	3.94 ⁷	2.20 ^{0.09} _{0.08}	5.90 ^{0.61} _{1.24}	2.60	2.00
M 3-34 ¹³	4.23	4.09 ¹³	3.93 ¹³			4.00 ^{0.01} _{0.01}	5.00
NGC 6543 ¹¹	4.20	4.14 ¹¹	3.83 ¹¹	4.00 ^{0.06} _{0.13}	3.20 ^{0.16} _{0.25}	4.20 ^{0.01} _{0.01}	3.90 ^{0.17} _{0.15}
NGC 6543 ¹²	4.20	3.90 ¹²	3.83 ¹²			2.70 ^{0.06} _{0.05}	2.80 ^{0.25} _{0.21}
NGC 6543 S ¹²	4.20	3.89 ¹²	3.83 ¹²			3.05 ^{0.04} _{0.07}	5.00 ^{0.29} _{0.85}
Hu 2-1 ¹³	4.00	3.99 ¹³	4.00 ¹³	4.30	2.00	4.20	5.00 ^{0.36} _{0.65}
M 1-73 ¹³	3.61	3.87 ¹³	3.74 ¹³			3.20 ^{0.01} _{0.03}	3.30 ^{0.11} _{0.11}
NGC 6302 ¹⁰	3.60	4.26 ¹⁰	4.21 ¹⁰	2.10	5.90	4.10 ^{0.16} _{0.21}	5.00 ^{0.08} _{0.17}
NGC 3132 ⁴	3.50	3.98 ⁴	4.03 ⁴	2.10	5.90 ^{0.01} _{0.01}	2.60	2.00
NGC 6302 ⁴	3.50	4.26 ⁴	4.21 ⁴	4.30	2.00	2.60	2.00
NGC 7026 ¹³	3.36	3.97 ¹³	3.87 ¹³	4.30 ^{0.11} _{0.51}	3.10 ^{0.36} _{0.70}	3.90 ^{0.08} _{0.13}	3.40 ^{0.06} _{0.13}
IC 1747 ¹³	3.20	4.04 ¹³	3.98 ¹³			3.80 ^{0.07} _{0.04}	5.00 ^{0.38} _{0.61}
IC 351 ¹³	3.14	4.12 ¹³	4.04 ¹³			3.90 ^{0.13} _{0.13}	3.20 ^{0.27} _{0.42}
NGC 6210 ¹²	3.10	3.98 ¹²	3.94 ¹²			3.05 ^{0.02} _{0.03}	5.00 ^{0.01} _{0.01}
Hu 1-1 ¹³	2.97	4.08 ¹³	3.92 ¹³			2.60 ^{0.63} _{0.32}	2.70 ^{0.40} _{0.22}
Sp 4-1 ¹³	2.94	4.05 ¹³	3.95 ¹³			4.00 ^{0.02} _{0.14}	2.75 ^{0.04} _{0.16}
IC 4846 ¹³	2.91	4.03 ¹³	3.89 ¹³				
IC 4846 ¹⁷	2.91	4.00 ¹⁷	4.26 ¹⁷	2.90 ^{0.66} _{0.75}	2.20	4.20 ^{0.03} _{0.04}	3.85 ^{0.21} _{0.15}
NGC 6803 ¹³	2.71	3.99 ¹³	3.93 ¹³			3.70 ^{0.07} _{0.27}	4.20 ^{0.37} _{0.27}
BoBn 1 ¹⁹	2.63	4.14 ¹⁹	3.95 ¹⁹	4.10 ^{0.03} _{0.04}	2.00 ^{0.12} _{0.03}	3.70 ^{0.26} _{0.23}	2.80 ^{0.22} _{0.35}
NGC 6833 ¹³	2.47	4.11 ¹³	4.15 ¹³			4.20 ^{0.21} _{0.64}	3.80 ^{0.17} _{0.40}
NGC 6879 ¹³	2.46	4.02 ¹³	3.93 ¹³			4.20	2.75 ^{0.04} _{0.02}
IC 4191 fixed ⁴	2.40	4.03 ⁴	4.02 ⁴	2.10	5.90	2.60	2.00
IC 4191 scanning ⁴	2.40	4.03 ⁴	4.02 ⁴	2.10	5.90	2.60	2.00 ^{0.01} _{0.01}
NGC 3132 ¹⁰	2.40	3.98 ¹⁰	4.03 ¹⁰	3.30 ^{0.12} _{0.14}	6.00 ^{0.49} _{0.76}	3.20 ^{0.34} _{0.12}	5.00 ^{0.15} _{0.99}
NGC 6720 ⁷	2.40	4.03 ⁷	3.90 ⁷	2.10 ^{0.05} _{0.03}	5.70 ^{0.31} _{0.37}	2.65 ^{0.05} _{0.05}	2.20 ^{0.07} _{0.06}

¹ Liu et al. (2000); ² Liu et al. (2001); ³ Ruiz et al. (2003); ⁴ Tsamis et al. (2003b); ⁵ Zhang & Liu (2003);⁶ Ercolano et al. (2004); ⁷ Liu et al. (2004); ⁸ Peimbert et al. (2004); ⁹ Sharpee et al. (2004); ¹⁰ Tsamis et al. (2004);¹¹ Wesson & Liu (2004); ¹² Robertson-Tessi & Garnett (2005); ¹³ Wesson et al. (2005); ¹⁴ Zhang et al. (2005a);¹⁵ Liu et al. (2006); ¹⁶ Sharpee et al. (2007); ¹⁷ Wang & Liu (2007); ¹⁸ García-Rojas et al. (2008); ¹⁹ Otsuka et al. (2010);²⁰ Wesson et al. (2003); ²¹ Fang & Liu (2011); ²² Esteban et al. (2002); ²³ Tsamis et al. (2003a); ²⁴ Esteban et al. (2004);²⁵ García-Rojas et al. (2004); ²⁶ García-Rojas et al. (2005); ²⁷ García-Rojas et al. (2006); ²⁸ García-Rojas et al. (2007);²⁹ López-Sánchez et al. (2007); ³⁰ Esteban et al. (2009); ³¹ Wesson et al. (2008); ³² Tsamis et al. (2008).

Table 1. (continued)

Object	From Literature			From Current Work			
	ADF (O ²⁺)	log T _e ([O III]) [K]	log T _e (BJ) [K]	log T _e (N II) [K]	log T _e (N II) [cm ⁻³]	log T _e (O II) [K]	log T _e (O II) [cm ⁻³]
NGC 6818 ¹⁰	2.40	4.12 ¹⁰	4.08 ¹⁰	3.20 ^{0.52}	6.00 ^{0.37} _{2.52}	2.95 ^{0.11} _{0.12}	4.75 ^{0.09} _{0.15}
IC 4191 nebula ¹⁰	2.40	4.03 ¹⁰	4.02 ¹⁰	3.80 ^{0.08} _{0.03}	2.70 ^{0.12} _{0.10}	3.80 ^{0.05} _{0.07}	3.90 ^{0.15} _{0.14}
IC 4191 fixed ¹⁰	2.40	4.03 ¹⁰	4.02 ¹⁰	3.80 ^{0.08} _{0.04}	2.70 ^{0.15} _{0.13}	3.25 ^{0.05} _{0.03}	4.05 ^{0.36} _{0.24}
IC 4191 ¹⁶	2.40	4.00 ¹⁶	3.90 ¹⁶	2.70 ^{0.09} _{0.05}	2.20 ^{0.02} _{0.16}	3.60 ^{0.05} _{0.01}	5.00
NGC 3918 ⁴	2.30	4.10 ⁴	4.09 ⁴	2.10 ^{0.01} _{0.01}	5.90 ^{0.04} _{0.04}	2.60 ^{0.04} _{0.01}	2.65 ^{0.12} _{0.21}
NGC 6884 ⁷	2.30	4.04 ⁷	4.06 ⁷	2.10 ^{0.01} _{0.03}	5.90 ^{0.21} _{0.24}	2.60	2.40 ^{0.01} _{0.02}
IC 5217 ¹³	2.26	4.05 ¹³	4.08 ¹³			3.50 ^{0.08} _{0.04}	5.00 ^{0.19} _{0.45}
NGC 3242 ¹⁰	2.20	4.07 ¹⁰	4.01 ¹⁰	4.00 ^{0.11} _{0.01}	2.50 ^{0.11} _{0.06}	3.35 ^{0.05} _{0.06}	5.00 ^{0.19} _{0.31}
NGC 5882 ⁴	2.20	3.97 ⁴	3.89 ⁴			2.60	3.10 ^{0.18} _{0.28}
M 1-74 ¹³	2.14	4.01 ¹³	3.89 ¹³			3.75 ^{0.30} _{0.32}	4.45 ^{0.53} _{0.32}
NGC 5882 ³²	2.14					2.95 ^{0.72} _{0.33}	2.40 ^{0.94} _{0.47}
NGC 5882 ¹⁰	2.10	3.97 ¹⁰	3.89 ¹⁰	3.90 ^{0.07} _{0.11}	3.00 ^{0.60} _{0.43}	3.55 ^{0.03} _{0.02}	5.00 ^{0.40} _{0.67}
Me 2-2 ¹³	2.10	4.04 ¹³	4.04 ¹³	3.80 ^{0.03} _{0.08}	2.20 ^{0.05} _{0.19}	4.00 ^{0.03} _{0.05}	5.00 ^{0.23} _{0.71}
NGC 7662 ⁷	2.00	4.13 ⁷	4.09 ⁷	2.10	5.90	2.60	2.00
NGC 5315 ¹⁰	2.00	3.95 ¹⁰	3.93 ¹⁰	3.80 ^{0.15} _{0.44}	4.70 ^{1.03} _{1.23}	4.00 ^{0.02} _{0.08}	4.30 ^{0.35} _{0.27}
NGC 6807 ¹³	2.00	4.04 ¹³	4.00 ¹³			4.00 ^{0.04} _{0.04}	3.15 ^{0.43} _{0.31}
NGC 5307 ³	1.95		4.03 ³			3.15 ^{0.15} _{0.15}	2.70 ^{0.60} _{0.34}
IC 4406 ⁴	1.90	4.00 ⁴	3.97 ⁴	2.10	5.90	2.60	2.20 ^{0.10} _{0.11}
IC 4406 ¹⁰	1.90	4.00 ¹⁰	3.97 ¹⁰	2.10 ^{0.01} _{0.01}	5.90 ^{0.05} _{0.06}	3.00 ^{0.08} _{0.04}	2.80 ^{0.07} _{0.17}
NGC 6741 ⁷	1.90	3.99 ⁷	4.15 ⁷	4.20 ^{0.34} _{0.35}	2.00 ^{0.84} _{0.17}	2.60	2.20
NGC 6826 ⁷	1.90	3.97 ⁷	3.94 ⁷	2.30 ^{0.35} _{0.13}	5.70 ^{0.41} _{0.12}	2.90 ^{0.01} _{0.02}	2.00 ^{0.02} _{0.02}
My Cn 18 ⁴	1.80	3.86 ⁴				2.60	2.15 ^{0.15} _{0.15}
My Cn 18 ¹⁰	1.80			4.30	2.00	3.25 ^{0.03} _{0.03}	2.50 ^{0.02} _{0.04}
NGC 3918 ¹⁰	1.80	4.10 ¹⁰	4.09 ¹⁰	4.00 ^{0.21} _{0.22}	2.70 ^{0.28} _{0.39}	2.60	2.00 ^{0.09} _{0.07}
NGC 7027 ¹²	1.80	4.15 ¹²	4.08 ¹²			2.65 ^{0.05}	2.00
NGC 7027 ¹⁴	1.80	4.10 ¹⁴	4.08 ¹⁴	3.90 ^{0.14} _{0.21}	3.10 ^{1.43} _{0.65}	4.00 ^{0.03} _{0.10}	5.00
NGC 5315 ⁸	1.74	3.95 ⁸	3.93 ⁸	4.30 ^{0.10}	6.00	4.20 ^{0.06} _{0.13}	4.95 ^{0.09} _{0.30}
NGC 6790 ⁷	1.70	4.11 ⁷	4.15 ⁷	2.10	5.90	2.60	2.20
NGC 6790 ¹²	1.70	4.11 ¹²	4.15 ¹²			2.60	2.00
Hu 1-2 ⁷	1.60	4.29 ⁷	4.30 ⁷	2.10	5.90	2.60	2.00
NGC 6572 ⁷	1.60	4.03 ⁷	4.01 ⁷	2.50 ^{0.59} _{0.06}	5.40 ^{0.29}	2.70 ^{0.01} _{0.05}	3.35 ^{0.07} _{0.43}
NGC 6572 ¹²	1.60	4.01 ¹²	4.01 ¹²			2.60 ^{0.05} _{0.01}	2.85 ^{0.47} _{0.07}
NGC 6572 S ¹²	1.60	4.01 ¹²	4.01 ¹²			2.60 ^{1.62}	2.30
NGC 6891 ¹³	1.52	3.97 ¹³	3.77 ¹³			4.20 ^{0.10} _{0.14}	3.30 ^{0.10} _{0.13}
NGC 5315 ⁴	1.40	3.95 ⁴	3.93 ⁴	2.10 ^{0.01} _{0.01}	5.90	2.90 ^{0.10} _{0.06}	5.00 ^{0.03} _{0.04}
M 3-32 ¹⁷	1.15	3.95 ¹⁷	3.65 ¹⁷	3.10 ^{0.20} _{0.22}	5.30 ^{0.47} _{0.47}	3.50 ^{0.06} _{0.02}	3.35 ^{0.11} _{0.11}
M 3-33 ¹⁷	1.10	4.02 ¹⁷	3.77 ¹⁷			3.60 ^{0.03} _{0.06}	3.25 ^{0.08} _{0.11}
IC 4699 ¹⁷	1.09	4.07 ¹⁷	4.08 ¹⁷	2.60 ^{1.11} _{0.23}	3.40 ^{1.41} _{0.93}	3.40 ^{0.10} _{0.12}	3.40 ^{0.23} _{0.16}
NGC 6439 ¹⁷	1.09	4.02 ¹⁷	4.00 ¹⁷	4.30 ^{0.01} _{0.01}	5.70 ^{0.19} _{0.01}	4.00 ^{0.01} _{0.01}	3.55 ^{0.19} _{0.12}
H 1-41 ¹⁷	1.08	3.99 ¹⁷	3.65 ¹⁷	2.90 ^{0.95} _{0.09}	4.80 ^{0.45} _{1.37}	3.45 ^{0.04} _{0.05}	2.10 ^{0.21} _{0.13}
M 3-7 ¹⁷	1.07	3.88 ¹⁷	3.84 ¹⁷	4.30	2.00	3.20 ^{0.24} _{0.11}	2.85 ^{0.27} _{0.26}
NGC 6620 ¹⁷	1.06	3.98 ¹⁷	4.00 ¹⁷	4.20 ^{0.04} _{0.52}	3.00 ^{0.05} _{0.74}	3.35 ^{0.08} _{0.02}	3.75 ^{0.19} _{0.16}
H 1-50 ¹⁷	1.05	4.04 ¹⁷	4.10 ¹⁷			3.15 ^{0.02} _{0.04}	2.85 ^{0.16} _{0.07}
H 1-54 ¹⁷	1.05	3.98 ¹⁷	4.10 ¹⁷	4.30	2.00	3.25 ^{0.32} _{0.20}	3.75 ^{0.32} _{0.24}
M 1-29 ¹⁷	1.05	4.03 ¹⁷	4.00 ¹⁷	3.00 ^{0.80} _{0.36}	3.40 ^{1.45} _{0.57}	2.60	2.00
M 3-21 ¹⁷	1.05	3.99 ¹⁷	4.04 ¹⁷	4.30 ^{0.02} _{0.02}	3.80 ^{1.41} _{0.36}	2.60	2.00
H 1-35 ¹⁷	1.04	3.96 ¹⁷	4.00 ¹⁷	4.30	2.00	3.20 ^{0.02} _{0.01}	4.75 ^{0.10} _{0.05}
H 1-42 ¹⁷	1.04	3.99 ¹⁷	4.00 ¹⁷	4.30	2.00	3.60 ^{0.03} _{0.07}	3.75 ^{0.43} _{0.30}
M 2-6 ¹⁷	1.04	4.00 ¹⁷	4.07 ¹⁷			3.80 ^{0.03} _{0.15}	5.00
M 2-27 ¹⁷	1.04	4.08 ¹⁷	4.15 ¹⁷	4.30	2.00	3.30 ^{0.29} _{0.17}	2.90 ^{0.18} _{0.20}
M 2-33 ¹⁷	1.04	3.91 ¹⁷	3.85 ¹⁷	3.30 ^{0.53} _{0.44}	2.50 ^{1.25} _{0.59}	2.60 ^{0.02} _{0.01}	3.60 ^{0.14} _{0.22}
M 2-42 ¹⁷	1.04	3.93 ¹⁷	4.15 ¹⁷	4.20 ^{1.71} _{0.15}	4.80 ^{1.88} _{0.32}	2.60	2.00
M 3-29 ¹⁷	1.04	3.96 ¹⁷	4.03 ¹⁷	3.10 ^{0.71} _{0.15}	5.30 ^{0.32} _{0.32}	2.60	2.00
NGC 6567 ¹⁷	1.04	4.02 ¹⁷	4.08 ¹⁷	4.30	2.00	2.80 ^{0.16} _{0.04}	3.05 ^{0.16} _{0.22}

¹ Liu et al. (2000); ² Liu et al. (2001); ³ Ruiz et al. (2003); ⁴ Tsamis et al. (2003b); ⁵ Zhang & Liu (2003);
⁶ Ercolano et al. (2004); ⁷ Liu et al. (2004); ⁸ Peimbert et al. (2004); ⁹ Sharpee et al. (2004); ¹⁰ Tsamis et al. (2004);
¹¹ Wesson & Liu (2004); ¹² Robertson-Tessi & Garnett (2005); ¹³ Wesson et al. (2005); ¹⁴ Zhang et al. (2005a);
¹⁵ Liu et al. (2006); ¹⁶ Sharpee et al. (2007); ¹⁷ Wang & Liu (2007); ¹⁸ García-Rojas et al. (2008); ¹⁹ Otsuka et al. (2010);
²⁰ Wesson et al. (2003); ²¹ Fang & Liu (2011); ²² Esteban et al. (2002); ²³ Tsamis et al. (2003a); ²⁴ Esteban et al. (2004);
²⁵ García-Rojas et al. (2004); ²⁶ García-Rojas et al. (2005); ²⁷ García-Rojas et al. (2006); ²⁸ García-Rojas et al. (2007);
²⁹ López-Sánchez et al. (2007); ³⁰ Esteban et al. (2009); ³¹ Wesson et al. (2008); ³² Tsamis et al. (2008).

Table 1. (continued)

Object	ADF (O ²⁺)	From Literature		From Current Work			
		log T_e ([O III]) [K]	log T_e (BJ) [K]	log T_e (N II) [K]	log T_e (N II) [cm ⁻³]	log T_e (O II) [K]	log T_e (O II) [cm ⁻³]
IC 4593 ¹²	1.03	3.92 ¹²	3.92 ¹²			2.80 ^{0.17} _{0.14}	2.00 ^{0.47} _{0.32}
He 2-118 ¹⁷	1.03	4.10 ¹⁷	4.26 ¹⁷	4.30	2.00	3.05 ^{0.05}	2.45 ^{0.21} _{0.18}
M 1-61 ¹⁷	1.03	3.95 ¹⁷	3.98 ¹⁷	4.00 ^{0.15} _{0.47}	2.30 _{0.76}	3.00	2.25 ^{0.02} _{0.06}
M 2-4 ¹⁷	1.03	3.93 ¹⁷	3.90 ¹⁷	4.00 ^{0.01} _{0.01}	2.00	4.20	3.45 ^{0.04} _{0.07}
NGC 6565 ¹⁷	1.03	4.01 ¹⁷	3.93 ¹⁷	4.30	2.00	3.35 ^{0.63} _{0.17}	3.05 ^{0.33} _{0.24}
Vy 2-1 ¹⁷	1.03	3.90 ¹⁷	3.94 ¹⁷	4.30	2.00	4.20 ^{0.02} _{0.05}	3.25 ^{0.05} _{0.03}
IC 418 ⁹	1.02	3.95 ⁹		4.20 ^{0.01} _{0.02}	2.30 ^{0.06} _{0.14}	4.20	3.85 ^{0.28} _{0.16}
Cn 1-5 ¹⁷	1.02	3.94 ¹⁷	4.00 ¹⁷	3.30 ^{0.09} _{0.07}	6.00 ^{0.42} _{0.54}	2.60	2.00
Cn 2-1 ¹⁷	1.02	4.01 ¹⁷	4.03 ¹⁷	3.40 ^{0.45} _{0.15}	6.00	3.25 ^{0.15} _{0.18}	3.75 ^{0.78} _{0.29}
M 1-20 ¹⁷	1.02	3.99 ¹⁷	4.08 ¹⁷			2.60 ^{0.01} _{0.01}	4.00 ^{0.13} _{0.15}
M 2-23 ¹⁷	1.02	4.08 ¹⁷	3.70 ¹⁷	4.30	2.00	4.15 ^{0.06} _{0.07}	5.00 ^{0.05} _{0.94}
IC 2501 ¹⁶	1.01	3.98 ¹⁶	3.85 ¹⁶	4.20 ^{0.03} _{0.08}	6.00 ^{0.31} _{1.88}	4.00 ^{0.06} _{0.03}	5.00 ^{0.02} _{0.02}
M 2-39 ¹⁷	0.95	3.91 ¹⁷	3.74 ¹⁷	4.10 ^{0.06} _{0.66}	5.80	2.65 ^{0.04} _{0.05}	2.60 ^{0.05} _{0.06}
Cn 3-1 ¹³		3.88 ¹³	3.71 ¹³	4.30	2.00		
M 2-31 ¹⁷		3.99 ¹⁷	4.15 ¹⁷				

⁹ Sharpee et al. (2004); ¹³Wesson et al. (2005); ¹⁶Sharpee et al. (2007); ¹⁷Wang & Liu (2007).

Table 2. Electron temperatures and densities for H II regions.

Object	From Literature		From Current Work				
	ADF (O ²⁺)	log T_e ([O III]) [K]	log T_e (BJ) [K]	log T_e (N II) [K]	log T_e (N II) [cm ⁻³]	log T_e (O II) [K]	log T_e (O II) [cm ⁻³]
SMC N87 ¹	2.80	4.09 ¹				2.60	2.20
M 17 ⁴	2.66	3.91 ⁴	3.89 ⁴	4.00 ^{0.16} _{0.41}	2.40 _{0.79}	2.60	2.00
LMC N141 ¹	2.60	4.07 ¹				2.60	2.00
NGC 3576 ⁴	2.21	3.95 ⁴	3.91 ⁴	3.30 ^{0.01}	6.00 ^{0.03} _{0.03}	2.60	2.00
30 Doradus ⁴	1.76	4.00 ⁴		3.30 ^{0.05} _{0.05}	6.00 ^{0.21} _{0.29}	2.60	2.00
LMC N66 ¹	1.61	4.26 ¹					
LMC N11 B ⁴	1.47	3.97 ⁴				2.60 ^{0.01} _{0.01}	2.00 ^{0.02} _{0.01}
PB 6-2 ²	1.12	4.18 ²					
PB 6-1 ²	1.10	4.20 ²					
PB 8 ²	1.05	3.84 ²	3.71 ²	2.10 ^{0.20} _{0.13}	5.80 ^{0.44} _{0.32}	4.20 ^{0.02} _{0.13}	3.30 ^{0.12} _{0.09}
NGC 2366 NGC 2363 ³	1.04	4.20 ³				2.85 ^{0.45} _{0.14}	2.90 ^{0.57} _{0.55}
NGC 3603 ⁸	1.04	3.96 ⁸				2.60 ^{0.01} _{0.01}	2.35 ^{0.02} _{0.09}
NGC 2867-2 ²	1.03	4.06 ²	3.95 ²			2.60	3.80 ^{0.21} _{0.39}
S 311 ⁷	1.03	3.95 ⁷	3.98 ⁷			2.60	2.00
M101 NGC 5461 ³	1.03	3.93 ³				3.15 ^{0.35} _{0.32}	4.65 ^{0.32} _{0.76}
M101 NGC 5471 ³	1.03	4.15 ³				2.85 ^{0.95}	4.40 ^{1.76} _{1.11}
M 42 ⁵	1.02	3.92 ⁵	3.90 ⁵	4.00 ^{0.07} _{0.02}	2.30 ^{0.09} _{0.05}	4.20 ^{0.06} _{0.08}	3.55 ^{0.11} _{0.14}
NGC 2867-1 ²	1.02	4.07 ²	3.95 ²			2.60	3.75 ^{0.21} _{1.40}
NGC 5253 HII-2 ¹⁰	1.01	4.08 ¹⁰				3.50 ^{0.19} _{0.24}	3.20 ^{0.33} _{0.33}
NGC 5253 UV-1 ¹⁰	1.01	4.04 ¹⁰				4.20 ^{0.07} _{0.70}	2.85 ^{0.55} _{0.33}
NGC 5253 HII-1 ¹⁰	1.00	4.08 ¹⁰				3.90 ^{0.17} _{0.67}	3.50 ^{0.42} _{0.57}
NGC 5253 UV-2 ¹⁰	1.00	4.04 ¹⁰					
M33 NGC 604 ³	1.00	3.91 ³				3.00 ^{0.03} _{0.04}	2.35 ^{0.10} _{0.10}
M33 NGC 604 ¹¹	1.00	3.91 ¹¹				2.60 ^{0.60} _{0.20}	2.00 ^{0.15} _{0.09}
M101 NGC 5461 ¹¹	0.99	3.93 ¹¹				3.35 ^{0.38} _{0.24}	2.65 ^{0.21} _{0.11}
NGC 2366 NGC 2363 ¹¹	0.97	4.20 ¹¹				3.65 ^{0.36} _{0.68}	2.00 ^{0.26} _{0.12}
M101 NGC 5447 ¹¹	0.97	3.93 ¹¹	3.82 ¹¹			3.05 ^{0.22} _{0.22}	2.15 ^{0.52} _{0.22}
SMC N66 ⁴	0.94	4.09 ⁴				2.60	2.00
NGC 3576 ⁶	0.91	3.95 ⁶	3.91 ⁶	2.10	5.90	3.50 ^{0.07} _{0.04}	2.75 ^{0.20} _{0.12}
NGC 4395 Reg 70 ¹¹	0.77	4.03 ¹¹				3.90 ^{0.16} _{0.13}	2.45 ^{0.17} _{0.22}
NGC 2403 VS 38 ¹¹	0.61	3.94 ¹¹				4.05 ^{0.02} _{0.32}	2.70 ^{0.02} _{0.46}
M 16 ⁸	0.45	3.88 ⁸	3.74 ⁸			3.00 ^{0.13} _{0.27}	2.60 ^{1.00} _{0.41}
NGC 2403 VS 24 ¹¹	0.45	3.91 ¹¹				3.70 ^{0.30} _{0.09}	2.40 ^{0.36} _{0.19}
NGC 1741 Zone C ¹¹	0.38	3.93 ¹¹				3.65 ^{0.40}	2.05 ^{0.69}
M 8 ⁹	0.37	3.91 ⁹	3.85 ⁹	2.10	5.90	3.15 ^{0.33} _{0.14}	2.50 ^{0.12} _{0.26}
M101 H1013 ¹¹	0.36	3.87 ¹¹				3.55 ^{0.44} _{0.37}	2.50 ^{0.20} _{0.23}
M33 NGC 595 ¹¹	0.34	3.87 ¹¹				3.70 ^{0.32} _{0.18}	2.55 ^{0.34} _{0.28}
M 20 ⁸	0.33	3.89 ⁸	3.78 ⁸			2.60	2.00
NGC 2403 VS 44 ¹¹	0.30	3.92 ¹¹				3.55 ^{0.40} _{0.29}	2.00 ^{0.18} _{0.09}
M 17 ⁹	0.27	3.91 ⁹		4.30	2.00	3.60 ^{0.42} _{0.17}	2.30 ^{0.52} _{0.27}
NGC 4861 BrightHII ¹¹	0.27	4.11 ¹¹				4.20 ^{0.59}	2.90 ^{0.64}
M31 K932 ¹¹	0.24	3.97 ¹¹				3.75 ^{0.36} _{0.66}	2.00 ^{0.36} _{0.13}

¹ Tsamis et al. (2003b); ² García-Rojas et al. (2008); ³ Esteban et al. (2002); ⁴ Tsamis et al. (2003a); ⁵ Esteban et al. (2004);

⁶ García-Rojas et al. (2004); ⁷ García-Rojas et al. (2005); ⁸ García-Rojas et al. (2006); ⁹ García-Rojas et al. (2007);

¹⁰ López-Sánchez et al. (2007); ¹¹ Esteban et al. (2009).

Table 3. The He I diagnostics from literature and current analysis for PNe.

Object	ADF(O ²⁺)	$T_e(\text{He I})$ [K]		
		$\frac{\lambda 7281}{\lambda 6678}$	$\frac{\lambda 6678}{\lambda 4471}$	$\frac{\lambda 6678}{\lambda 5876}$
Abell 30 J3 ²⁰	766.0		9080	8230
Abell 30 J1 ²⁰	598.0		5830	3910
Abell 58 ³¹	89.0		587	1250
Hf 2-2 (2 arcsec) ¹⁵	84.0		1070	1570
Hf 2-2 (4 arcsec) ¹⁵	84.0			840
Hf 2-2 (8 arcsec) ¹⁵	84.0		816	1460
NGC 1501 ⁶	32.0	4800 ⁶	5100 ⁶	4100 ⁶
M 1-42 ²	22.0	3790	2500	2380
NGC 40 ⁷	17.3		7430	5470
M 2-24 ⁵	17.0			4500
NGC 2022 ⁴	16.0		19700	6980
NGC 2022 ¹⁰	16.0		15900 ¹⁰	
DdDm 1 ¹³	11.8			3500 ¹³
NGC 6153 ¹	9.2	3260	10600	5570
IC 2003 ¹³	7.3		1600 ¹³	7670 ¹³
M 2-36 ²	6.9	2710	3420	4370
Vy 1-2 ¹³	6.2		3550 ¹³	4430 ¹³
NGC 3242 ⁴	5.7	4620	9290	7120
NGC 2440 ¹⁶	5.4	10400	7430	4500
NGC 6818 ⁴	4.9	3420	5270	5880
NGC 7009 ²¹	4.7	5030	9670	4310
IC 3568 ⁷	4.6		15900	10900
NGC 6210 ⁷	4.3		9470	10600
M 3-34 ¹³	4.2		17000 ¹³	
NGC 6543 ¹¹	4.2	6610	8440	5560
M 1-73 ¹³	3.6		8820 ¹³	7960 ¹³
NGC 6302 ¹⁰	3.6		15100 ¹⁰	
NGC 3132 ⁴	3.5	10800	14500	10800
NGC 6302 ⁴	3.5			5010
NGC 7026 ¹³	3.4		4050 ¹³	4120 ¹³
IC 351 ¹³	3.1		3790 ¹³	4600 ¹³
Hu 1-1 ¹³	3.0		9550 ¹³	4740 ¹³
Sp 4-1 ¹³	2.9		3150 ¹³	2400 ¹³
IC 4846 ¹³	2.9		13400 ¹³	
IC 4846 ¹⁷	2.9	8890	5880	2490
NGC 6803 ¹³	2.7		8100 ¹³	4840 ¹³
BoBn 1 ¹⁹	2.6	9430 ¹⁹	5580	1590
NGC 6833 ¹³	2.5		14100 ¹³	2440 ¹³
NGC 6879 ¹³	2.5		3750 ¹³	2340 ¹³
IC 4191 fixed ⁴	2.4	5850	3080	2050
IC 4191 scan ⁴	2.4	8340	2890	1920
NGC 3132 ¹⁰	2.4		13900 ¹⁰	
NGC 6720 ⁷	2.4		13300	10300
NGC 6818 ¹⁰	2.4		5000 ¹⁰	
IC 4191 neb ¹⁰	2.4		3000 ¹⁰	
IC 4191 fixed ¹⁰	2.4		2800 ¹⁰	
NGC 3918 ⁴	2.3	7320	15700	7730
NGC 6884 ⁷	2.3			8990
IC 5217 ¹³	2.3		5100 ¹³	3000 ¹³
NGC 3242 ¹⁰	2.2		10000 ¹⁰	
NGC 5882 ⁴	2.2	5380	10300	6840
M 1-74 ¹³	2.1		9200 ¹³	3380 ¹³

Table 3. (Continued)

Object	ADF(O ²⁺)	$T_e(\text{He I})$ [K]		
		$\frac{\lambda 7281}{\lambda 6678}$	$\frac{\lambda 6678}{\lambda 4471}$	$\frac{\lambda 6678}{\lambda 5876}$
NGC 5882 ¹⁰	2.1		10700 ¹⁰	
NGC 7662 ⁷	2.0		4830	3550
NGC 5315 ¹⁰	2.0		10000 ¹⁰	
NGC 6807 ¹³	2.0			1000 ¹³
NGC 5307 ³	1.9	8050	6040	4360
IC 4406 ⁴	1.9	5260	7620	4600
IC 4406 ¹⁰	1.9		8000 ¹⁰	
NGC 6741 ⁷	1.9		19400	6720
NGC 6826 ⁷	1.9		8510	8310
My Cn 18 ⁴	1.8	4740		7670
NGC 3918 ¹⁰	1.8		12000 ¹⁰	
NGC 7027 ¹⁴	1.8	10500 ¹⁴	8260	1970
NGC 5315 ⁸	1.7	7910	7180	4350
NGC 6790 ⁷	1.7			10600
Hu 1-2 ⁷	1.6			12800
NGC 6572 ⁷	1.6			7420
NGC 6891 ¹³	1.5		4100 ¹³	3660 ¹³
NGC 5315 ⁴	1.4	6090	9220	5580
M 3-32 ¹⁷	1.1	1710 ¹⁷	3620	2970
M 3-33 ¹⁷	1.1	4960	4190	2970
IC 4699 ¹⁷	1.1	2290	6540	5170
NGC 6439 ¹⁷	1.1	5180	2270	2010
H 1-41 ¹⁷	1.1	2700	6310	5100
M 3-7 ¹⁷	1.1	2340	7390	2610
NGC 6620 ¹⁷	1.1	3720	2570	2490
H 1-50 ¹⁷	1.1	7990	8230	3140
H 1-54 ¹⁷	1.1	6650	18800	5210
M 1-29 ¹⁷	1.1	2940	5430	2750
M 3-21 ¹⁷	1.1	6430	3740	2570
H 1-35 ¹⁷	1.0	11000	3870	1830
H 1-42 ¹⁷	1.0	7310	3130	1990
M 2-6 ¹⁷	1.0	7870	4100	2870
M 2-27 ¹⁷	1.0	2760	7630	3990
M 2-33 ¹⁷	1.0	4530	7740	4880
M 2-42 ¹⁷	1.0	3370	7240	5990
M 3-29 ¹⁷	1.0	1800 ¹⁷	5990	4450
NGC 6567 ¹⁷	1.0	10400	7100	2590
He 2-118 ¹⁷	1.0	10600	15600	4360
M 1-61 ¹⁷	1.0	6070	18500 ¹⁷	13200
M 2-4 ¹⁷	1.0	8400	4060	4160
NGC 6565 ¹⁷	1.0	4770	6470	5470
Vy 2-1 ¹⁷	1.0	5000	5140	4330
IC 418 ⁹	1.0		4440	4040
Cn 1-5 ¹⁷	1.0	2740	11600	7360
Cn 2-1 ¹⁷	1.0	6500	5180	2210
M 1-20 ¹⁷	1.0	7800	3850	1800
M 2-23 ¹⁷	1.0	10300	4860	1830
IC 2501 ¹⁶	1.0	9130	8400	4130
M 2-39 ¹⁷	0.9	7790	6090	5600
Cn 3-1 ¹³	0.0		4700 ¹³	3400 ¹³
M 2-31 ¹⁷	0.0	4390	2170	1770

¹ Liu et al. (2000); ² Liu et al. (2001); ³ Ruiz et al. (2003); ⁴ Tsamis et al. (2003b); ⁵ Zhang & Liu (2003);⁶ Ercolano et al. (2004); ⁷ Liu et al. (2004); ⁸ Peimbert et al. (2004); ⁹ Sharpee et al. (2004); ¹⁰ Tsamis et al. (2004);¹¹ Wesson & Liu (2004); ¹² Robertson-Tessi & Garnett (2005); ¹³ Wesson et al. (2005); ¹⁴ Zhang et al. (2005a);¹⁵ Liu et al. (2006); ¹⁶ Sharpee et al. (2007); ¹⁷ Wang & Liu (2007); ¹⁸ García-Rojas et al. (2008); ¹⁹ Otsuka et al. (2010);²⁰ Wesson et al. (2003); ²¹ Fang & Liu (2011); ²² Esteban et al. (2002); ²³ Tsamis et al. (2003a); ²⁴ Esteban et al. (2004);²⁵ García-Rojas et al. (2004); ²⁶ García-Rojas et al. (2005); ²⁷ García-Rojas et al. (2006); ²⁸ García-Rojas et al. (2007);²⁹ López-Sánchez et al. (2007); ³⁰ Esteban et al. (2009); ³¹ Wesson et al. (2008); ³² Tsamis et al. (2008).

Table 4. Electron temperatures of H II regions derived from the He I recombination lines.

Object	ADF(O ²⁺)	$T_e(\text{He I})$ [K]		
		$\frac{\lambda 7281}{\lambda 6678}$	$\frac{\lambda 6678}{\lambda 4471}$	$\frac{\lambda 6678}{\lambda 5876}$
M 17 ³	2.7	19000	7940	5050
LMC N141 ¹	2.6	14900	6570	
NGC 3576 ³	2.2		10500	6500
30 Doradus ³	1.8	12400	5350	5490
LMC N66 ¹	1.6		3630	
LMC N11 B ³	1.5		4740	1930
PB 6-2 ²	1.1		15200	15900
PB 6-1 ²	1.1			15400
PB 8 ²	1.1	6760	6940	11100
NGC 3603 ⁷	1.0	11500	13900	8800
NGC 2867-2 ²	1.0	9810	4750	3760
S 311 ⁶	1.0	9190	7150	7480
M 42 ⁴	1.0	6700	4860	2880
NGC 2867-1 ²	1.0	11500	6550	6640
NGC 5253 HII-2 ⁹	1.0	8440	6150	7440
NGC 5253 UV-1 ⁹	1.1	6230	7990	5220
NGC 5253 HII-1 ⁹	1.0		6720	4320
NGC 5253 UV-2 ⁹	1.0		5210	2820
M33 NGC 604 ¹⁰	1.0			17400
M101 NGC 5461 ¹⁰	1.0	5320		
M101 NGC 5447 ¹⁰	1.0		10400	4770
SMC N66 ³	0.9		12600	
NGC 3576 ⁵	0.9	10300		
M 16 ⁷	0.4	8380	6350	5410
M 8 ⁸	0.4	7380	6240	6790
M101 H1013 ¹⁰	0.4	4330		
M33 NGC 595 ¹⁰	0.3	2110	6560	6280
M 20 ⁷	0.3	8870	5660	6180
M 17 ⁸	0.3	6120	5590	6690

¹ Tsamis et al. (2003b); ² García-Rojas et al. (2008); ³ Tsamis et al. (2003a); ⁴ Esteban et al. (2004); ⁵ García-Rojas et al. (2004);

⁶ García-Rojas et al. (2005); ⁷ García-Rojas et al. (2006); ⁸ García-Rojas et al. (2007); ⁹ López-Sánchez et al. (2007);

¹⁰ Esteban et al. (2009);